ADVANCING EARTH AND SPACE SCIENCES

JGR Planets

RESEARCH ARTICLE

10.1029/2023JE008270

Key Points:

- Dayside O_3 column abundances on Mars between MY 34 (L_S = 150°) and MY 36 have been obtained using the NOMAD-UVIS instrument
- Ozone is strongly correlated with the presence of water ice clouds in the aphelion season
- Differences between observed and modeled ozone diurnal variations points toward an under/overestimation of water ice condensation

Supporting Information:

Supporting Information may be found in the online version of this article.

Correspondence to:

J. P. Mason,
jon.mason@open.ac.uk

Citation:

Mason, J. P., Patel, M. R., Holmes, J. A., Wolff, M. J., Alday, J., Streeter, P., et al. (2024). Climatology and diurnal variation of ozone column abundances for 2.5 Mars years as measured by the NOMAD-UVIS spectrometer. *Journal of Geophysical Research: Planets*, *129*, e2023JE008270. https://doi.org/10.1029/2023JE008270

Received 12 JAN 2024
Accepted 27 MAR 2024

Author Contributions:

Conceptualization: J. P. Mason
Data curation: J. P. Mason, B. Ristic
Formal analysis: J. P. Mason, M. R. Patel, J. A. Holmes, J. Alday, K. S. Olsen
Funding acquisition: M. R. Patel
Investigation: J. P. Mason, J. A. Holmes
Methodology: J. P. Mason, J. Alday
Project administration: M. R. Patel, I. Thomas, A. C. Vandaele
Resources: M. R. Patel
Software: J. P. Mason, M. J. Wolff, G. Sellers
Supervision: M. R. Patel
Validation: J. P. Mason, M. J. Wolff
Visualization: J. P. Mason, J. A. Holmes, C. Marriner
Writing – original draft: J. P. Mason

Climatology and Diurnal Variation of Ozone Column Abundances for 2.5 Mars Years as Measured by the NOMAD-UVIS Spectrometer

J. P. Mason[1], M. R. Patel[1,2], J. A. Holmes[1], M. J. Wolff[3], J. Alday[1], P. Streeter[1], K. S. Olsen[1,4], M. A. J. Brown[1,5], G. Sellers[1], C. Marriner[1], Y. Willame[6], I. Thomas[6], B. Ristic[6], F. Daerden[6], A. C. Vandaele[6], J.-J. Lopez-Moreno[7], and G. Bellucci[8]

[1]School of Physical Sciences, The Open University, Milton Keynes, UK, [2]Space Science and Technology Department, Science and Technology Facilities Council (STFC), Rutherford Appleton Laboratory, Didcot, UK, [3]Space Science Institute, Boulder, CO, USA, [4]Department of Physics, University of Oxford, Oxford, UK, [5]Yusuf Hamied Department of Chemistry, Centre for Atmospheric Science, University of Cambridge, Cambridge, UK, [6]Royal Belgian Institute for Space Aeronomy (BIRA-IASB), Brussels, Belgium, [7]Instituto de Astrofísica de Andalucía (IAA), Consejo Superior de Investigaciones Científicas (CSIC), Granada, Spain, [8]Istituto di Astrofisica e Planetologia Spaziali, INAF, Rome, Italy

Abstract The distribution of Mars ozone (O_3) is well established; however, our knowledge on the dayside diurnal variation of O_3 is limited. We present measurements of Mars O_3 column abundances, spanning Mars Year (MY) 34 to the end of MY 36, by the Ultraviolet and VIsible Spectrometer (UVIS), part of the Nadir and Occultation for MArs Discovery (NOMAD) instrument, aboard the ExoMars Trace Gas Orbiter. UVIS provides the capability to measure dayside diurnal variations of O_3 and for the first time, a characterization of the dayside diurnal variations of O_3 is attempted. The observed O_3 climatology for Mars Years (MY) 34–36 follows the established seasonal trends observed through previous O_3 measurements. At aphelion, the equatorial O_3 distribution is observed to be strongly correlated with the water ice distribution. We show that the early dust storm in MY 35 resulted in a near-global reduction in O_3 during northern spring and the O_3 abundances remained 14% lower in northern summer compared to MY36. Strong latitudinal and longitudinal variation was observed in the diurnal behavior of O_3 around the northern summer solstice. In areas with a weak O_3 upper layer, O_3 column abundance peaks in the mid-morning, driven by changes in the near-surface O_3 layer. In regions with greater O_3 column abundances, O_3 is observed to gradually increase throughout the day. This is consistent with the expected diurnal trend of O_3 above the hygropause and suggests that in these areas an upper O_3 layer persists throughout the Martian day.

Plain Language Summary Ozone, a highly reactive gas, plays an important role in the chemical cycles of both carbon and hydrogen on Mars. As ozone is tightly correlated to the presence of the difficult to detect odd hydrogen species, measurement of the ozone distribution can provide vital insight into the Martian photochemistry. We present the ozone abundances measured by the UVIS spectrometer aboard the ExoMars Trace Gas Orbiter, spanning Mars years (MYs) 34–36 and attempt to characterize the daily variations in ozone. The ozone follows the expected seasonal trends, with the highest ozone abundances observed at polar regions in the spring, autumn and winter seasons of both hemispheres and very little ozone during southern summer, outside the northern polar latitudes. An enhancement in equatorial ozone during northern summer is observed, with MY 35 showing lower ozone abundances compared to MY 36, likely the effect of an early dust storm in MY 35 or the long-term impact of the MY 34 global dust storm. In both years, the O_3 distribution in northern summer appears to closely follow the water ice distribution and the observed daily cycle in ozone is shown to be highly sensitive to the presence of a high altitude ozone layer.

1. Introduction

The Ultraviolet and VIsible Spectrometer (UVIS), part of the Nadir and Occultation for MArs Discovery (NOMAD) instrument (Vandaele et al., 2018) aboard the ExoMars Trace Gas orbiter (TGO), has been operating around Mars since March 2018 and has provided near continuous radiometric measurements between 200 and 650 nm of the surface and atmosphere (Patel et al., 2017). The inversion of the UVIS radiance spectra around the Hartley band (Hartley, 1881) provides the spatial and temporal (seasonal and diurnal) variation of ozone (O_3), a highly photochemically reactive gas that can be used as a tracer for other minor species that are difficult to

Writing – review & editing: M. R. Patel, J. A. Holmes, M. J. Wolff, J. Alday, P. Streeter, K. S. Olsen, M. A. J. Brown, C. Marriner, Y. Willame, I. Thomas

observe, such as odd hydrogen species, namely the highly reactive hydroxyl radicals (HO, HO_2, H_2O_2, collectively known as HO_x). This coupling between the O_3 and HO_x abundances makes the monitoring of O_3 a valuable tool for understanding photochemistry in the martian atmosphere for example, (Clancy & Nair, 1996; Lefèvre et al., 2004, 2008; Montmessin & Lefèvre, 2013).

In the atmosphere of Mars, O_3 is created through the recombination of oxygen (O_2) and molecular oxygen (O), which are produced by the photolysis of carbon dioxide (CO_2) and O_3 from incident sunlight (Lefèvre et al., 2004; Nair et al., 1994; Shimazaki & Shimizu, 1979). While photolysis is responsible for initializing the production of O_3 in the atmosphere of Mars, the absorption of photons at UV wavelengths also results in the destruction of O_3, with the strongest absorption peaking around 255 nm, a spectral region known as the Hartley band (Hartley, 1881). The other O_3 destruction mechanism is from interactions with HO_x, which are the products of water vapor photolysis (Lefèvre et al., 2004; Marmo et al., 1965; Modak et al., 2019; Shimazaki & Shimizu, 1979). The coupling between HO_x and O_3 leads to the well-documented photochemical anti-correlation between O_3 and water vapor and the simultaneous monitoring of these two end member species enables a better understanding of HO_x, which not only control the relative abundances of O_3, but also the overall stability of CO_2 in the atmosphere of Mars (Clancy & Nair, 1996; Perrier et al., 2006). Subsequently, the strong relationship between O_3 and water vapor has been used to validate the photochemistry of short-lived species (Clancy et al., 2016; Lefèvre et al., 2021), and, by extension, the water vapor cycle (Daerden et al., 2019; Holmes et al., 2018; Lefèvre et al., 2008; Montmessin & Lefèvre, 2013) as well as being used as a tracer to track the global circulation (Holmes et al., 2017).

The first detection of O_3 in the martian atmosphere was in the southern polar region in 1969 by Mariner 7 during a flyby mission (Barth et al., 1973). In 1972, Mariner 9 mapped the seasonal variation of O_3 and since then the geographical and vertical O_3 distribution has been monitored throughout multiple Martian years by instruments on different missions. This includes: the SPectroscopy for the Investigation of the Characteristics of the Atmosphere of Mars (SPICAM) aboard the Mars Express orbiter (Bertaux et al., 2004; Lebonnois et al., 2006; Lefèvre et al., 2021; Määttänen et al., 2013, 2022; Modak et al., 2019; Perrier et al., 2006; Willame et al., 2017); the Mars Color Imager (MARCI) on the Mars Reconnaissance Orbiter (MRO; Bell et al., 2009; Clancy et al., 2016), the Imaging UltraViolet Spectrograph (IUVS) aboard Mars Atmospheric and Volatile EvolutioN orbiter (MAVEN; Braude et al., 2023; Gröller et al., 2018; McClintock et al., 2015), NOMAD (Khayat et al., 2021; Patel et al., 2021; Piccialli et al., 2023) and the Atmospheric Chemistry Suite (ACS) also on TGO (Korablev et al., 2018; Olsen et al., 2020, 2022). As well as direct measurement of the dayside O_3 abundance and distribution, observation of $O_2(a^1\Delta_g)$ emission has allowed indirect measurement of the dayside O_3 abundance and distribution (see Clancy et al., 2017; Fedorova et al., 2006; Guslyakova et al., 2016). These measurements, together with modeling efforts, have led to a good understanding of O_3 photochemistry, including its spatial distribution and seasonal variations (e.g., Brown et al., 2022; Clancy & Nair, 1996; Holmes et al., 2018; Lefèvre et al., 2004, 2008, 2021; Montmessin et al., 2017; Nair et al., 1994).

Variations in O_3 are strongly linked to changes in the water vapor conditions that are in turn associated with large latitudinal and seasonal variations in the atmospheric temperature driven by orbital variations. Due to its elliptical orbit, compared to the northern summer season, Mars receives ∼45% more solar insolation in the southern summer season when Mars is at perihelion ($L_S \sim 251°$), warming the atmosphere. Warmer temperatures suppress the formation of water ice clouds and increase the hygropause altitude (the altitude at which water condenses), allowing water vapor to be transported more efficiently to the northern hemisphere. This increase in atmospheric water at equatorial latitudes leads to a decrease in O_3 with the column abundances reaching a seasonal minimum (<2 μm-atm) (Lefèvre et al., 2021). The largest O_3 abundances have been observed in the winter polar regions of each hemisphere, where the cold atmospheric temperatures lead to the condensation of a large fraction of the water vapor mass onto the seasonal water ice frosts. The absence of water vapor and O_3 photolysis (i.e., no sunlight) results in O_3 column abundances that can exceed 50 μm-atm at the poles (Lefèvre et al., 2021). Strong longitudinal variations in the O_3 column over short-timescales (∼3–4 sols) were observed in the northern polar region (>60°N) by MRO/MARCI and were associated with perturbations of the polar vortex by transient waves bringing colder and dryer air to lower latitudes (Clancy et al., 2016).

During aphelion (northern summer), when the atmosphere is colder, the formation of the aphelion cloud belt in the equatorial region decreases the abundance of water vapor, and restricts the transport of water vapor to southern latitudes, allowing O_3 abundance to increase. The lower altitude hygropause at aphelion results in the formation of two distinct layers in O_3; one below the hygropause, and the other at higher altitudes above the hygropause (Braude et al., 2023; Gröller et al., 2018; Khayat et al., 2021; Lebonnois et al., 2006; Lefèvre et al., 2004; Määttänen et al., 2013, 2022; Montmessin & Lefèvre, 2013; Olsen et al., 2020; Patel et al., 2021; Piccialli et al., 2023). Enhanced O_3 column abundances have also been observed near large topographical features throughout the aphelion season, such as the Hellas and Argyre Basins. Clancy et al. (2016) show that the concentration within the Hellas basin is observed to peak twice: once during southern winter, $L_S = 50°–100°$, where ozone total column values reached up to 25 μm-atm; and also in early southern spring, $L_S = 130°–160°$, with strong interannual variations in the O_3 column abundances from ∼10 to ∼30 μm-atm. Model simulations suggest that the first peak is due to the meridional transport of O_3 -rich air from the north (Clancy et al., 2016), while the second peak results from the transport of southern polar air toward the equatorial regions later in the season when water ice at the polar cap sublimates (Clancy et al., 2016).

While past measurements have given a comprehensive understanding of the O_3 spatial and seasonal distribution, the local time coverage has been limited to either fixed local times on the dayside as in the case of MARCI nadir observations, snapshots of the O_3 vertical distributions at discrete local times and locations from solar/stellar occultations (Braude et al., 2023; Khayat et al., 2021; Määttänen et al., 2013, 2022; Patel et al., 2021; Piccialli et al., 2023), or in the case for SPICAM nadir observations, the distinction between measurement time was not reported. Our understanding of the O_3 dayside diurnal cycle, therefore, comes from 1-D photochemical models (Nair et al., 1994) or 3-D photochemical models that are linked to Global Climate Model (GCM) simulations (see Lefèvre et al., 2004, 2008).While dayside variations in the O_3 column abundance are expected to be small, Lefèvre et al. (2004) showed that the largest daytime variations in O_3 may be found in the lower 3 km of the atmosphere, where the photolysis of NO_2 leads to an increased abundance of O atoms and thus an increase in O_3 which peaks in the mid-morning around 1000 LST. In the upper O_3 layer that forms during aphelion, the rapid increase of O with altitude and the fast recombination into O_3 is believed to cause significant diurnal variations (Lefèvre et al., 2004). For the first time, we attempted to characterize the O_3 diurnal variation utilizing the local time variation of the UVIS measurements.

In this paper, we present the O_3 column abundances retrieved from UVIS radiance measurements. The UVIS dataset spans from $L_S = 150°$ (MY 34) through to the end of MY 36. Section 2 provides details of UVIS and its observational characteristics and Section 3 details the retrieval scheme and model assumptions. In Section 4, we provide an uncertainty analysis and validation of UVIS O_3 column abundance results against MARCI O_3 columns. Finally, Section 5 describes the O_3 climatology for MY 34, MY 35 and MY 36 and analysis of the O_3 diurnal variations in the MY 35 aphelion season.

2. UVIS Observations

The TGO orbit is approximately circular, with a periapsis of 380 km and apoapsis of 420 km and an inclination of 74°. The 2 hr orbital period allows 12 dayside nadir passes per day and, because the TGO orbit is not a sun-synchronous, UVIS is able to make multiple measurements at different local solar times (LST) as the nadir track moves across different latitudes. Full coverage of the surface achieved after 373 orbits (approximately 1 month), when the orbit "closes" (i.e., repeats the same ground track), providing near global data. The ∼74° inclined orbit of TGO prevents observations of O_3 poleward of 75°.

A nominal UVIS dayside nadir campaign lasts about an hour and consists of >100 individual nadir observations of the surface, with the measurement cadence (and thus the number of total observations) dependent on the selected integration time for the orbit (i.e., each observation within an orbit has the same integration time). The integration time is generally set based on the minimum solar zenith angle (θ_z) along the nadir track, calculated using the SPICE toolkit (Acton, 1996; Acton et al., 2018), to prevent saturation of the visible wavelengths. Based on this requirement, the integration time was set to 5 s for $\theta_z < 40°$, 7 s for $\theta_z < 60°$, and 10 s or 20 s for $\theta_z > 60°$. Approximately 10% of the observations were allocated as "UV optimized," where the integration time was fixed to 10 s or 20 s, independent of θ_z, in order to maximize the UV signal at the expense of potential saturation at longer visible wavelengths (>550 nm); this saturation is not a concern for this study, which focuses solely on the UV wavelength region. The different integration times result in a shorter or longer projected footprint on the Mars surface, with a footprint length typically between ∼15 km (5 s) and ∼60 km (20 s). The width of the footprint is independent of integration time and is typically around 5 km.

10.1029/2023JE008270

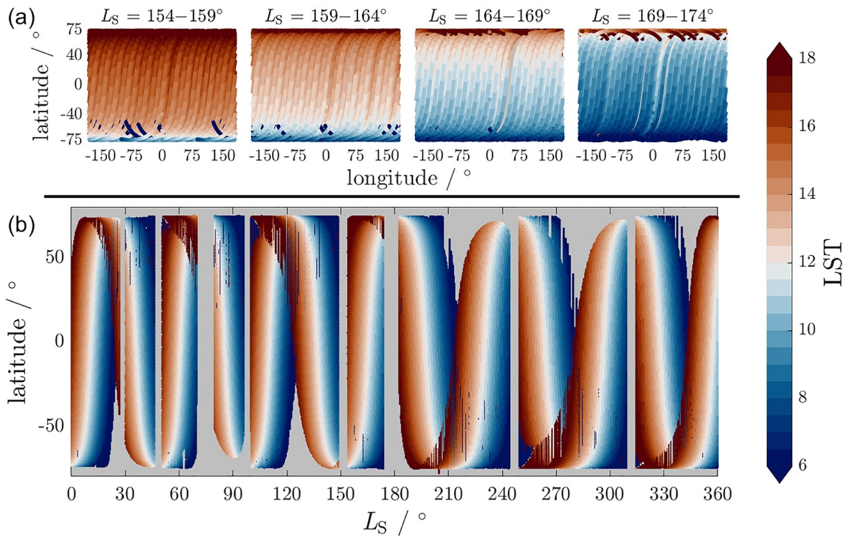

Figure 1. The dayside UVIS ground-tracks and the evolution of local solar time (LST) as a function of (a) latitude and longitude between $L_S = 154°–174°$ in MY 35 and (b) latitude and L_S for the UVIS nadir observations in MY 35 for $\theta_z \leq 70°$ For MY 34 and MY 36, the LST dependence on latitude, longitude, and L_S is similar to MY 35.

Figure 1 shows the ground-tracks and illustrates the precession of the observation local solar time (LST) as a function of latitude, longitude, and solar longitude (L_S) for the UVIS observations in MY 35. Also note that Figure 1 only shows part of the ground-tracks where $\theta_z \leq 70°$, a limit imposed by the plane-parallel assumption in the retrieval scheme (see Section 3.1). The evolution of LST with time (moving by ~26 min per 1° of L_S at the equator) results in the observed two-phase pattern where UVIS alternates between observing the afternoon and morning sides of the planet. Sampling of the diurnal cycle from 0730 to 1630 LST equates to a period of approximately $L_S = 26°$ at the equator. Over a single dayside orbit the LST exhibits a latitudinal dependence, starting either at sunrise (sunset) at high latitudes in either the southern or northern hemisphere and progressing toward sunset (sunrise) as TGO migrates to the opposite hemisphere.

The UVIS observations used in this study were processed and calibrated as described by Mason et al. (2022) and Willame et al. (2022). A duty cycle (i.e., not continuous operation) of 50% (i.e., cut half of all nadir observations) was implemented from June 2020 for UVIS observations corresponding to $L_S = 219°$ in MY 35 to prolong the life of the instrument through the extended mission phase. While the O_3 climatology can still be mapped, the reduction in the number of different local times sampled in a given area is significantly reduced. This was because the priority was to achieve a spatially uniform observation distribution to enable UVIS to achieve climatology aims rather than uniform coverage of LST. The reduced number of observations in MY36 coupled with unfavorable solar zenith angles (i.e., > 70°—where we cannot perform our retrieval, see Section 3.1) in the time period over which we perform the diurnal analysis (see Section 5.2) limits our ability to perform a diurnal analysis in MY36. Therefore, in this study, we limit the diurnal analysis to earlier in MY 35 only, prior to the duty cycle implementation.

3. O_3 Retrieval Method

In the following sections we outline our retrieval scheme, which follows in a similar vein to previous O_3 retrievals (e.g., Clancy et al., 2016; Lefèvre et al., 2021; Willame et al., 2017), whereby a radiative transfer (RT) code is used to simulate radiances from a model atmosphere. Key parameters are iterated within the model atmosphere until the modeled and measured radiances agree. In the following sections, the radiative transfer code, the a priori dataset used to construct the model Mars atmosphere, and the adopted optical properties of the surface, dust and ice aerosols are described. Finally, we end this section with an overview of the retrieval procedure.

3.1. Radiative Transfer

The radiative transfer (RT) analysis is performed using the Discrete Ordinates Radiative Transfer (DISORT) package (Stamnes et al., 2000; Thomas & Stamnes, 2002) to simulate the Martian radiances in the 220–320 nm spectral range. Here, we employ the "front-end" routines (DISORT_MULTI), for studies of the Martian atmosphere, to generate the input grids and parameters required by DISORT (Clancy et al., 2016; Wolff et al., 2009, 2010, 2019). The scattering calculations are performed assuming a plane-parallel atmosphere; therefore, we limit our retrievals to observations where the solar zenith angle <70° to minimize the error introduced by this assumption. We employ 16 streams to ensure accurate estimates of the scattering field and the atmosphere is divided into 21 discrete layers between 0 and 80 km with layer thickness of 1 km near the surface, 2 km between 2 and 22 km, 5 km between 25 and 50 km and 10 km above 60 km. We use version 2 of the Total and Spectral Solar Irradiance Sensor (TSIS)-1 Hybrid Solar Reference Spectrum (HSRS) (Coddington et al., 2023) as our solar irradiance input required for DISORT, which has a stated uncertainty in our wavelength range of 1.3%.

3.2. The a Priori Atmosphere

Recent coincident observations of the water vapor and O_3 vertical profiles by NOMAD and ACS (Aoki et al., 2022; Olsen et al., 2022; Patel et al., 2021) have shown the criticality of water vapor along with temperature in driving the seasonal and spatial variations in the vertical distribution of O_3. We therefore use the reanalysis dataset from OpenMARSv1 (Holmes et al., 2020, 2022a) to create our a priori atmosphere to achieve an accurate representation for the vertical distribution of Mars O_3 for our retrievals.

This reanalysis dataset was created using an assimilation scheme that integrates observational atmospheric data into the UK spectral version of the Planetary Climate Model (PCM UK-spectral) (Forget et al., 1999; Lewis et al., 2007). The Holmes et al. (2022b) reanalysis dataset incorporates the water vapor vertical distributions spanning L_S = 150–360° in MY 34 from ACS and NOMAD (Aoki et al., 2019; Fedorova et al., 2020), temperature profiles and dust column data from the Mars Climate Sounder (MCS) aboard MRO (Kleinböhl et al., 2017; McCleese et al., 2007),as well as temperature profiles from ACS (Fedorova et al., 2022). To obtain priors beyond MY 34, the assimilation was continued but only included the MCS temperature and column dust optical depth (CDOD).

To construct the vertical profiles of pressure, temperature, water ice, dust, and ozone, we linearly interpolated the model output fields both spatially and temporally to match the UVIS observation location and time. This provided a unique set of vertical profiles for each UVIS observation constrained by position, season, and local time. To account for differences between the model topography and high-resolution topography data measured by the Mars Orbiter Laser Altimeter (Abramov & McEwen, 2004; Smith et al., 2001), model sigma levels were converted to altitude coordinates prior to interpolation, and a correction was applied to the surface pressure field. This pressure correction was necessary to accurately model the Rayleigh scattering contribution to the reflectance below 260 nm. Since it directly impinges on the Hartley band absorption, a too high/low assumed pressure profile could lead to an over/underestimation of the O_3 column. The a priori CDOD and O_3 column abundances, required by the retrieval, were found by vertically integrating the corresponding altitude profiles.

3.3. Surface Reflectance

Since UVIS is not capable of distinguishing between ice clouds (H_2O or CO_2) and surface ice, whereby both result in a brightening of the nadir observed spectrum, we consider a two-surface approach depending on whether they are flagged as icy or non-icy.

In the nominal case of a non-icy surface, we use the Hapke surface parameterization derived by Wolff et al. (2019). In this case, the surface is described by a two-lobe Henyey-Greenstein phase function with Hapke parameter values of: $[b = 0.27, c = 0.7, B0 = 1.0, h = 0.06, \overline{\theta} = 20]$ which define the asymmetry parameter, backward scattering fraction, opposition effect width, opposition effect amplitude, and the macroscopic roughness. Except for the albedo, the Hapke parameters are assumed constant for all UVIS measurements. Wolff et al. (2019) used MARCI data to derive a Hapke UV reflectance map for MARCI band 7 (321 nm) and applied a scaling factor to estimate the albedo in band 6 (263 nm). We apply a similar approach here to derive a wavelength dependant albedo over the wavelength range 215–320 nm. First, we interpolate the UVIS observation location onto the MARCI band 7 albedo map to obtain the 321 nm albedo and use the scaling factor derived by Wolff et al. (2019) to estimate the albedo at 263 nm. We use linear interpolation to determine the albedo at all wavelengths between 263 and 321 nm. At wavelengths shorter than 263 nm, given the lack of available data, we assume a constant surface albedo set to the value at 263 nm. To account for changes in the surface albedo over time and the coarse resolution of the albedo map, which could lead to incorrect surface albedos for observations close to surface dichotomies, we allow the surface albedo to vary within 20% of the values derived by Wolff et al. (2019).

At high latitudes, we define a surface ice boundary using a modified version of the polar cap regression defined by Wolff et al. (2019). Based on this spatial constraint, we flag any observation within this ice boundary (see Figures S1 and S2 in Supporting Information S1) that had a Lambertian reflectance $A_L = I/F/\cos(\theta_i) > 0.04$ as an ice surface. In the retrieval, we assume a Lambertian surface for observations that are flagged as observing a potential ice surface and the water ice optical depth (τ_{ice}) is set to 0 and not retrieved. A full discussion on how we defined the ice boundary and why we chose an A_L cut-off of 0.04 is given in Supporting Information S1. Outside the polar ice boundary, a Lambertian surface was flagged for observations with $A_L > 0.09$; above this value, water ice clouds alone were found to be insufficient to accurately account for the bright radiances observed by UVIS.

3.4. Dust and Water Ice Aerosols

For the dust aerosols, we use the recently derived dust optical properties by Connour et al. (2022) using IUVS/MAVEN data, who used a similar method as described by Wolff et al. (2010) to obtain the dust refractive indices at UV wavelengths and a derived set of self-consistent optical properties for different dust particle size distributions using T-matrix calculations (Mishchenko et al., 2002). In all retrievals, we applied a single parameterization for the dust particle optical properties, assuming a gamma distribution for the particle size distribution with moments: effective radius (r_{eff}) = 1.8 and effective variance (v_{eff}) = 0.1 (Wolff, et al., 2009,2010). To define the optical properties for water ice clouds, we assume that the ice particles are described by a single size distribution with moments r_{eff} = 3.0 μm and v_{eff} = 0.1 and employ the optical properties and scattering phase function of a droxtal shape as described in Wolff et al. (2019).

3.5. Retrieval Procedure

Computational limitations meant that we could not fit the entirety of the UVIS data between 220 and 320 nm at the UVIS resolution of ~2 nm. Instead, we binned the radiance factor (I/F) into 9 spectral bins centered at [220., 228., 247., 258., 267., 289., 305., 310., 320.] nm and a width of ±2 nm. The central wavelengths were found by finding the spectral bins that resulted in the lowest standard deviations, that is, the lowest variations between adjacent pixels and helped to avoid visible solar lines in our I/F such as the MG II lines. Averaging the I/F across several pixels in each spectral bin also reduced the impact of single pixel events on our retrieval., The shorter two wavelengths in our selected range are most sensitive to the dust component and Rayleigh scattering, while the longer wavelengths >305 nm are primarily sensitive to water ice with the central wavelengths used to derive the O_3 column abundance.

The retrieval scheme is summarized in the steps below where we use an iterative procedure to obtain values for the O_3 column abundance, the dust and water ice optical depths, and surface albedo.

1. Compute the I/F from the UVIS radiances using the HSRS solar spectrum.
2. Average the computed I/F into the pre-selected spectral bins.
3. Create the a priori atmosphere using the inputs from the OpenMARSv1 reanalysis dataset (Section 4.2).
4. Compute A_L and set the surface as icy/non-icy based on the constraints detailed in Section 3.3.
5. Calculate and generate the required input files for DISORT.
6. Call the retrieval procedure which uses the MPFIT minimization package (Markwardt, 2009) to iterate the O_3 column abundance, dust and water ice optical depths and albedo until the modeled I/F converges to the measured I/F.

Convergence of the retrieval procedure, defined to be when the absolute difference between modeled and measured I/F is within 1%, generally occurs after 5–10 iterations. Figure 2 provides four examples of the spectral fit to the UVIS radiance data for a range of O_3 column abundances (1.5, 5, 12, and 25 μm-atm) that are representative of the O_3 abundances seen on Mars. In general, the developed retrieval scheme achieves good convergence with the residuals between the measured and modeled spectra within the measurement uncertainty in each case.

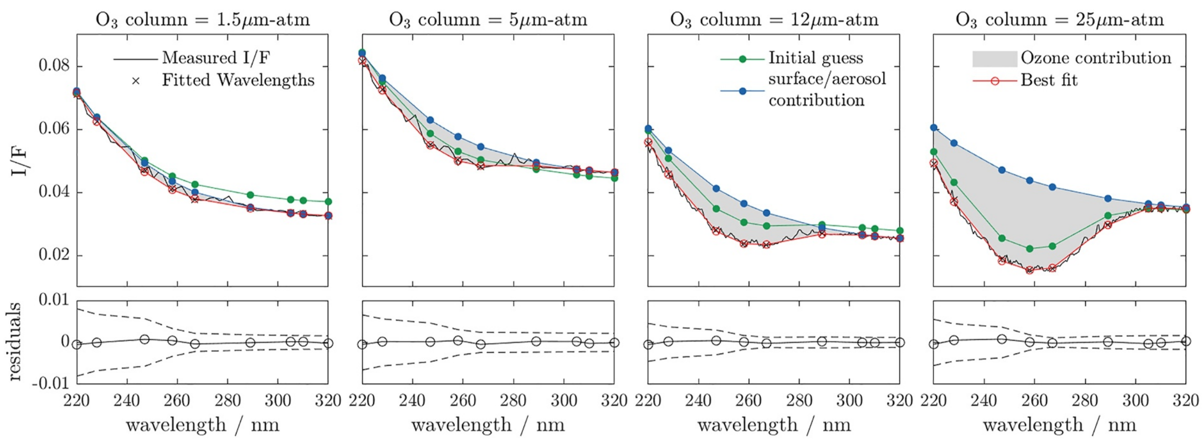

Figure 2. Examples of the spectral fits to the UVIS radiance data for a range of O_3 column abundances. The black lines show the measured UVIS radiances with the fitted wavelengths shown by the open black circles. The initial guess for the retrieval is shown in green and the blue line shows the contribution of the surface albedo and aerosols. The ozone contribution is shown by the gray shaded area with the best fit is represented by the red line. The lower row of plots rows the residuals between the model and measured I/F with dashed lines indicating the uncertainty.

4. Filtering, Uncertainty, and Validation

4.1. Filtering and False Detections of O_3

Our retrieval fits four parameters, surface albedo, dust optical depth, water ice optical depth, and the ozone column using the MPFIT minimization package, which uses the Marquardt-Levenberg algorithm to find the best fit values for our four parameters (Markwardt, 2009). The uncertainty in our retrieved values is provided by the diagonal of the covariance matrix, an output of the MPFIT package.

When the RT model fits ozone abundances below 0.5 μm-atm, our retrieval becomes increasingly insensitive to ozone, evidenced by large uncertainties (>100%) in our retrieved values. Following the method outlined by Daerden et al. (2022), we apply the filter $(O_{3,\mathrm{col}} + 0.01)/\delta O_{3,\mathrm{col}} > 1$, where $O_{3,\mathrm{col}}$ is the retrieved O_3 column abundance and $\delta O_{3,\mathrm{col}}$ is the uncertainty in the retrieved value. The addition of a small amount of O_3 (0.01) is to help distinguish from measurements which are undetectable due to noise/error and measurements which have a low error but produce negligible O_3. Another common problem when using the Hartley band to retrieve O_3 in high dust loading conditions is the false detection of O_3, leading to apparent high O_3 abundances during perihelion (e.g., Clancy et al., 2016; Lefèvre et al., 2021; Willame et al., 2017). To remove these artifacts from the O_3 data we re-ran all the retrievals a second time but with the O_3 column abundance kept constant at 0 and compared the resulting chi-squared (χ^2) against those from the nominal retrieval., Again following Daerden et al. (2022), we apply the filter $\chi^2_{O_3}/\chi^2_{no,O_3} < 1$, to our entire dataset where $\chi^2_{O_3}$ and χ^2_{no,O_3} are the measure of the fit quality with and without O_3 retrieved respectively (i.e., removed any retrieval where good fits were observed with or without O_3 fitted). We also discard any O_3 result coinciding with a retrieved dust optical depth >2.0 to avoid O_3 false detections resulting from high dust abundances.

The result of the data filtering was the removal of approximately 24% of the UVIS observations (not including the θ_z threshold which results in ~36% of the observations being excluded due to the plane-parallel assumption in the RT code) and, as the histogram in Figure 3a shows, the majority of those observations rejected (84%) have O_3 abundances <0.4 μm-atm. The seasonal and latitudinal distributions of the accepted and rejected observations are shown Figures 3b and 3c, which provide the number of observations as a function of L_S and latitude, respectively. Most of the rejected observations are in regions and seasons associated with low O_3 columns, that is, at mid-southern and equatorial latitudes in spring, autumn, and summer in the southern hemispheres. The accepted observations show the opposite trend with a bias toward the aphelion season and high polar latitudes. There is a bias toward the northern hemisphere in the accepted observations that we attribute to the higher O_3 abundances observed in the northern spring compared to the southern spring at mid and poleward latitudes.

10.1029/2023JE008270

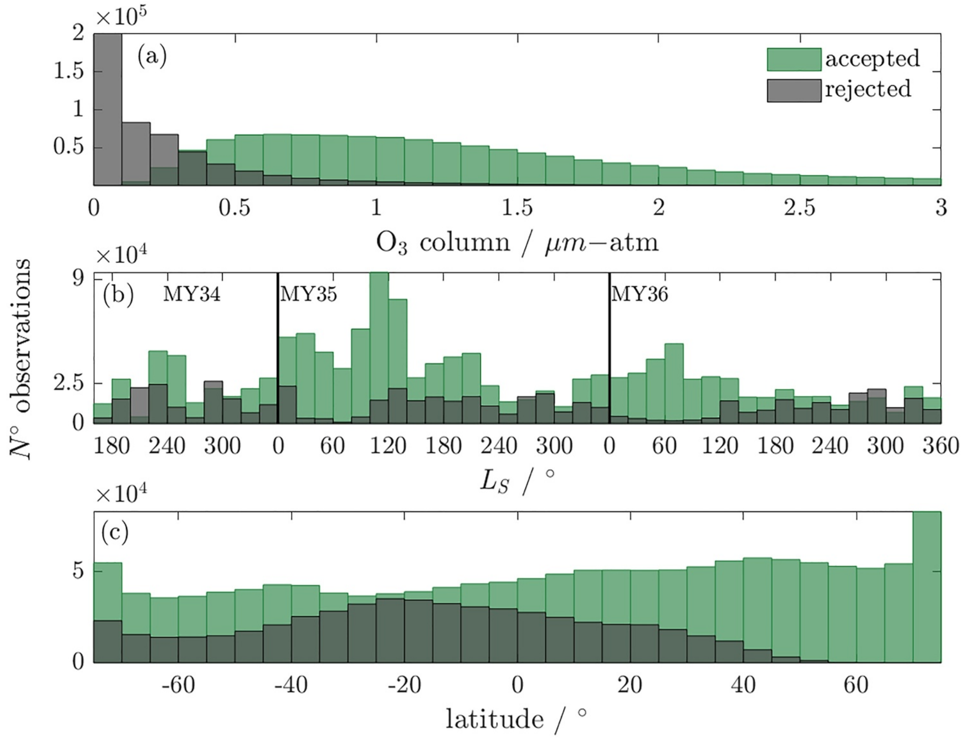

Figure 3. Histograms showing the number of observations accepted (green) and rejected (gray) as a function of (a) O_3 column abundance, (b) season in terms of L_S, and (c) latitude.

4.2. Uncertainty Analysis

In order to understand the systematic uncertainties in the retrieved O_3 column abundances retrieved from UVIS spectra, we calculated the correlated errors induced by biases in the rest of the atmospheric model parameters. The uncertainties in the UVIS O_3 column abundances associated with the Rayleigh scattering-induced uncertainties arising from surface pressure ($\tau_{Rayleigh}$), the dust and ice optical depth (τ_{dust} and τ_{ice}), the surface albedo (ω_{surf}), and radiance measurement error $I/F(\lambda)_{err}$ are given in Table 1 for low (1 μm-atm), medium (5 μm-atm), and high (20 μm-atm) O_3 abundances. For the uncertainty analysis, after application of the acceptance criteria described in the previous section, all UVIS observations with a column abundance of 1 ± 0.05 μm-atm, 5 ± 0.05 μm-atm, and 20 ± 0.05 μm-atm were found and 200 observations were selected randomly from each bin to ensure a range of different surface and atmospheric conditions, and to avoid selective biases. For each of the selected observations,

Table 1
Summary of the Uncertainties (μm-atm) in the Retrieved O_3 Column Abundances From Uncertainty in the Input Parameters, Retrieved Parameters, and Measurement Error

Parameter (error source)	O_3 column = 1 μm-atm	O_3 column = 5 μm-atm	O_3 column = 20 μm-atm
P_{surf} (1%)[a]	±0.1	±0.1	±0.3
τ_{dust} (20%)[b]	±0.3	±0.3	−0.7, +1.6
τ_{ice} (30%)[b]	±0.3	−0.7, +0.4	±1.0[c]
ω_{surf} (5%)[b]	±0.2	±0.4	±2.0
Radiance (λ)[d]	−0.7, +0.8	−0.8, +0.9	−2.7, +3.3

[a]The error in the OpenMARSv1 surface pressure was found to be 1% (Mischna et al., 2022). [b]The average uncertainty across all the selected observations. [c]τ_{ice} uncertainty at high O_3 abundance was found for observations typically around the Hellas basin at aphelion. At higher latitudes, the majority of the observations are flagged as a Lambertian surface where the τ_{ice} retrieval is turned off. [d]This error terms relate to the wavelength dependent uncertainty relative to the average uncertainty from 300 to 320 nm and ranged from <5% at 255 nm to <12% at 220 nm.

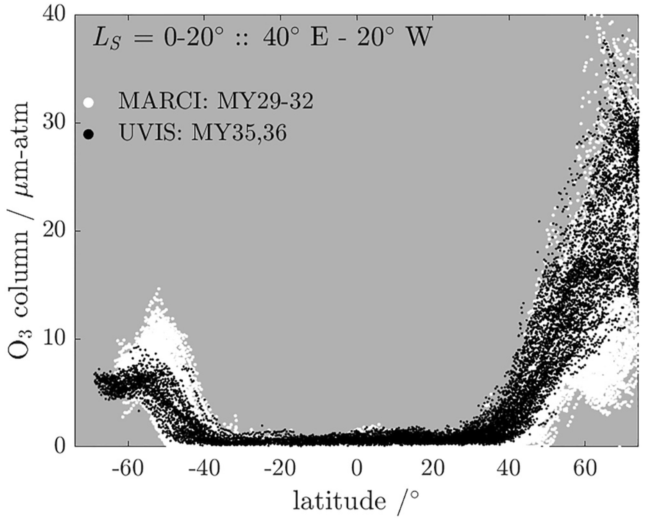

Figure 4. A comparison of ozone column latitudinal dependence retrieved by UVIS in MY 35 and MY 36 against those by MARCI for MY28-32 (Clancy et al., 2016) over the period L_S = 0°–20° and between 40°E–20°W.

the errors associated with each quantity were derived using a Monte Carlo approach whereby each parameter (τ_{Rayleigh}, τ_{dust}, τ_{ice}, ω_{surf}, and input radiance $I/F(\lambda)$) was randomly varied, in turn, within their uncertainties (with the uncertainty for $\tau_{\mathrm{dust,\ ice}}$ and ω_{surf} coming directly from the O_3 retrieval) and fixed (i.e., not retrieved in the case of τ_{dust}, τ_{ice}, ω_{surf}). The retrieval code was re-run to obtain a new O_3 column abundance each time a parameter was iterated, and to ensure sufficient statistics, each parameter was randomly varied 200 times for all of the selected observations. A representative uncertainty is then found by taking the average of the maximum and minimum O_3 column abundance found for each of the observations in each bin.

The uncertainties in the retrieved O_3 column abundances by UVIS as a result of the uncertainties in the input and retrieved parameters are relatively small and typically <0.5 μm-atm. At moderate O_3 abundances (i.e., 5 μm-atm), the uncertainty in the O_3 column abundances is more sensitive to τ_{ice} which is likely forced by the fact that the location where we observed such O_3 values coincides with areas we would typically expect surface frost to form, that is, the water ice clouds could be overcompensating for a brighter surface. For high O_3 abundances, the uncertainty in the surface reflectance becomes the dominant source of uncertainty. High O_3 abundances are typically observed at high polar latitudes in the spring, autumn, and winter season where surface ice coverage and solar zenith angles are high, making the retrieval highly sensitive to the surface parametrization. The dominant error source comes from the uncertainty in the measured radiance, which, across the UV, increases from ~5% at 320 nm up to ~15% at 220 nm and typically ~8% at 255 nm in the middle of the Hartley band. This error leads to uncertainties in the retrieved O_3 abundances that are typically <0.8 μm-atm for low and moderate abundances and typically <3 μm-atm for high O_3 abundance.

4.3. Validating UVIS O_3 Against MARCI O_3

The high degree of repeatability in the seasonal variation of O_3 allows for a comparison between the UVIS O_3 in MY 35–36 to those measured by MARCI for MY29-MY32 (Clancy et al., 2016) to provide a qualitative validation of the UVIS O_3 dataset. The aim of this comparison was to investigate systematic bias in the UVIS data that could result from residual straylight in the spectrum partially masking the Hartley band. Figure 4 shows the O_3 latitudinal distribution between L_S = 0°–20° spanning a longitudinal range from 20°W to 40°E measured by UVIS and MARCI. While a certain amount of inter-annual variation is expected, we see no systematic bias in the UVIS data and good agreement between the UVIS and MARCI O_3 columns is seen at all latitudes, with peak ozone values near 45 μm-atm in the northern hemisphere, approximately 10 μm-atm in the southern hemisphere and minimal ozone at the equator.

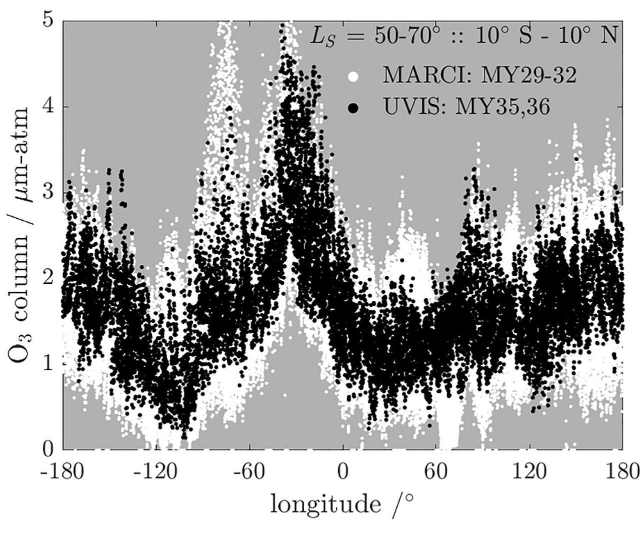

Figure 5. The longitudinal dependence of O_3 at the equator between L_S = 50°–70° retrieved by UVIS in MY 35 and MY 36 against those by MARCI for MY28-32 (Clancy et al., 2016).

The weak interannual variability and strong longitudinal dependence of the aphelion O_3 (Clancy et al., 2016) provide a unique case for testing UVIS O_3 under low and highly variable O_3 conditions. Any bias in the data, resulting from residual straylight, will be immediately evident with UVIS failing to resolve the expected longitudinal distribution. In Figure 5, we compare the measured O_3 columns by UVIS and MARCI as a function of longitude for the aphelion period L_S = 50°–70°. The equatorial longitudinal distribution and magnitude of O_3 is well resolved by UVIS with no systematic bias seen in the UVIS dataset and good qualitative agreement with MARCI is observed. The spread of O_3 values in the UVIS dataset is somewhat narrower than for MARCI, which we attribute to the reduced coverage of UVIS, that is, ~10,000 datapoints for MY 35 and MY 36 versus >80,000 datapoints for MARCI over MY 29–MY 32.

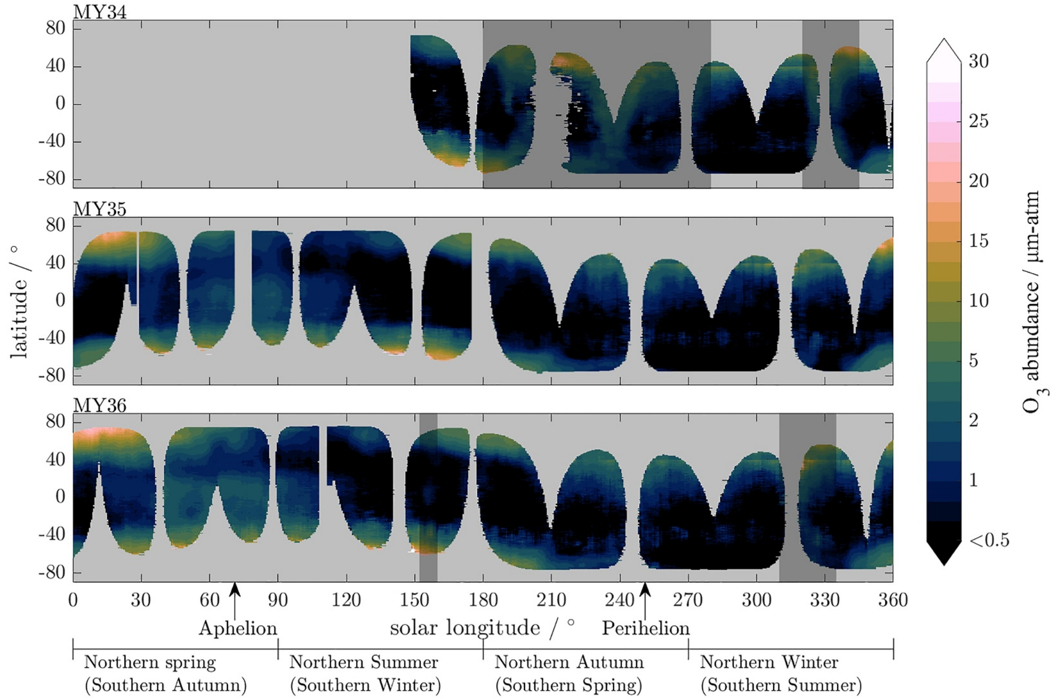

Figure 6. The zonally averaged column abundances of O_3 as a function of L_s and latitude for MY 34 (L_S = 150°–360°) top panel, MY 35 middle panel and MY 36 bottom panel. Only observations with a solar zenith angle <70° are shown and we have blacked out time periods that contain false ozone detections as a result of high dust loading.

The agreement with MARCI O_3 and the lack of any observed systematic bias in the UVIS data supports our assumption that any potential residual straylight has a negligible impact on our retrieved O_3 columns and validates our UVIS O_3 retrievals.

5. Retrieved UVIS O_3 Column

5.1. Ozone Climatology

The UVIS O_3 dataset begins in the southern spring season (L_S = 150°) of MY 34 (the start of the TGO science phase) with observations processed until the end of MY 36, providing the global O_3 distribution for approximately 2.5 Mars years. In Figure 6 we present the zonally averaged retrieved O_3 columns from UVIS as a function of season (L_S) and latitude with MY 34 shown in the top panel, MY 35 in the middle panel, and MY 36 in the bottom panel. The plots were produced by binning the data into L_S and latitude bins of 3° by 2°, with between ∼20 and ∼100 observations in each latitude bin spaced uniformly across all longitudes. The well-established seasonal trends in Mars O_3 columns are observed by UVIS for all Mars Years. The largest O_3 columns are seen consistently at the edges of the weakly illuminated polar regions in the spring, autumn and winter hemisphere, associated with cold atmospheric temperatures and low water vapor abundance (water vapor condensing to form clouds). The depletion of O_3 in the perihelion season at equatorial latitudes is observed in all Mars years, where the warmer temperatures suppress the condensation of water vapor into clouds, leading to an overall increase in the water vapor abundance, and by extension HO_x that destroy O_3. The observed seasonal distribution in O_3 is seen to be well correlated to the seasonal variations of the $O_2(a^1\Delta_g)$ emission measured by SPICAM (Fedorova et al., 2006). The winter, spring and autumn hemispheres show the strongest O_2 emission, mirroring the O_3 distribution shown in Figure 6. In the SPICAM data, enhanced O_2 emission is also apparent at equatorial latitudes in the aphelion season, where we also see a buildup of O_3.

A low latitude O_3 enhancement during the northern hemisphere summer is seen in both MY 35 and MY 36 and is a consequence of a colder atmosphere resulting from reduced solar insolation due to the increased Mars-Sun distance. In both years, the increase in low latitude O_3 coincides with the formation of the Aphelion Cloud Belt (ACB), a band of cloud at mid and equatorial latitudes that wraps around Mars (e.g., Clancy et al., 1996;

10.1029/2023JE008270

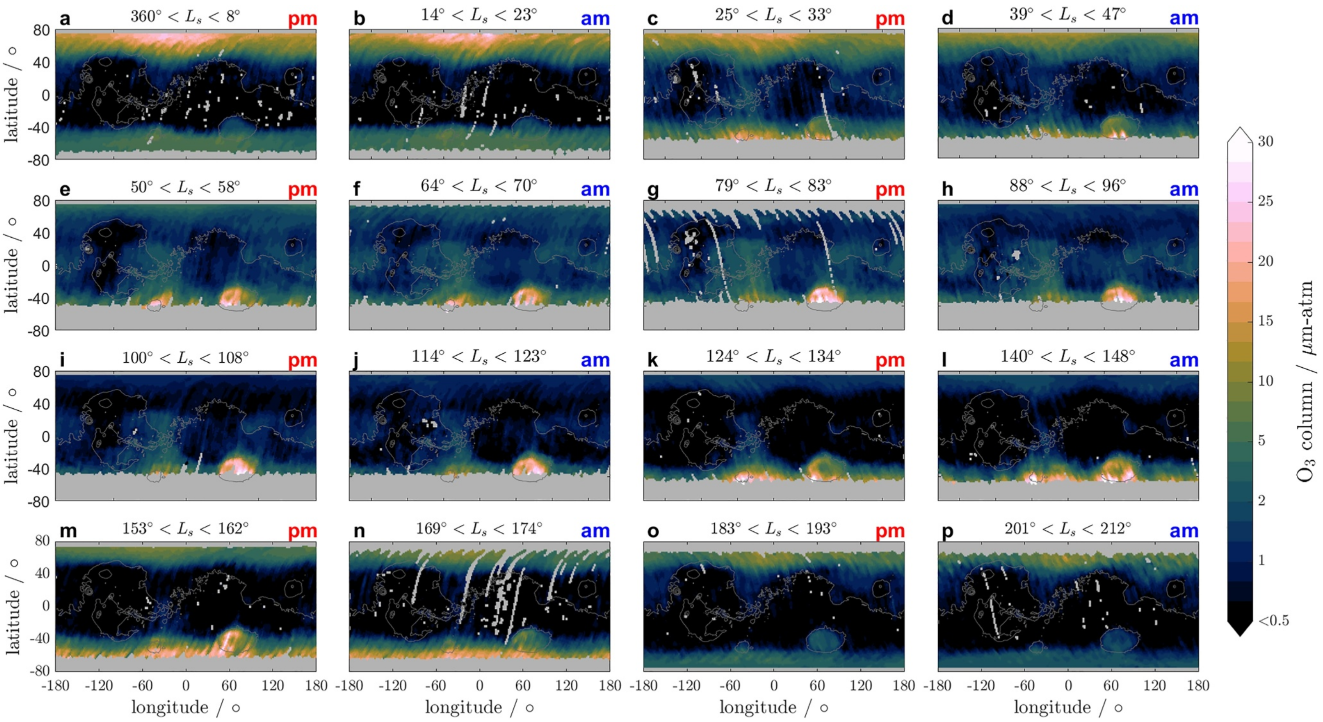

Figure 7. The geographical distribution of ozone for MY 35 between L_S = 0–212°. Each panel alternates between the afternoon and morning atmosphere that is, panels (a, c, e, g, i, k, m, o), represent local solar times between 1200 LST and 1800 LST and panels (b, d, f, h, j, l, n, p) present the morning retrievals from 0600 LST to 1200 LST. The irregular L_S periods and the gaps in L_S are due to the orbital coverage and the beta angle causing no observations, respectively. Note the color scale in non-linear to highlight lower O_3 columns.

Guha et al., 2021; Mateshvili et al., 2007; Pearl et al., 2001; Wolff et al., 2019, 2022). An in-depth discussion and climatological maps showing the distribution and evolution of the ACB can be found in the literature (see, Giuranna et al., 2021; Olsen et al., 2021; Smith, 2004, 2009, Wolff et al., 1999). The ACB begins to form in northern spring around the same time we see the increase in low latitude O_3, and signifies the freezing of water vapor to form water ice clouds as the atmosphere cools, allowing O_3 to build-up. The peak in the aphelion O_3 precedes the peak in the ACB and is observed to occur around the time when Mars reaches aphelion ($L_S \sim 71°$).

UVIS provides sufficient spatial coverage to produce averaged geographical maps representing the afternoon (PM) and morning (AM) O_3 columns over a ∼16 sol period. The O_3 maps (generated using 1° × 1° bin averages) for the aphelion season, beginning at the northern spring equinox ($L_S \sim 0°$) through to $L_S \sim 212°$ in MY 35 and $L_S \sim 223°$ for MY 36, are presented in Figures 7 and 8 for MY 35 and MY 36, respectively. The first MY 35 map (a) in Figure 7 shows the PM atmosphere, with subsequent maps alternating between AM and PM. Conversely, the first map (a) in Figure 8 for MY 36 shows the AM atmosphere and alternates in the opposite order.

High northern latitudes: Spring in the northern high latitudes around $L_S = 0°$ shows the largest abundances in O_3, with a peak abundance of ∼40 μm-atm, in good agreement with previous O_3 studies (Clancy et al., 2016; Lefèvre et al., 2021; Willame et al., 2017). These large O_3 abundances are associated with very low atmospheric water vapor abundances forced by cold atmospheric temperatures. The O_3 column abundances in the northern polar regions have been observed to have large day-to-day variations driven by perturbations in the polar vortex by transient planetary waves (Clancy et al., 2016; Lefèvre et al., 2004; Wilson, 2002). The short timescales (few sols) of these transient waves are not resolved in the UVIS maps, which are averaged over ∼16 sols. However, the prominent stationary wave structure is observed and gives rise to the strong longitudinal dependence in O_3 with the highest abundances in the polar region observed between 100°W and 40°E. The O_3 column abundances in the high northern latitudes reach a minimum during northern summer between L_S = 90°–125° associated with an increase in low altitude water vapor abundance (Clancy & Nair, 1996; Lefèvre et al., 2004; Olsen et al., 2022). In northern autumn, colder atmospheric temperatures and the encroachment of the polar night to lower latitudes

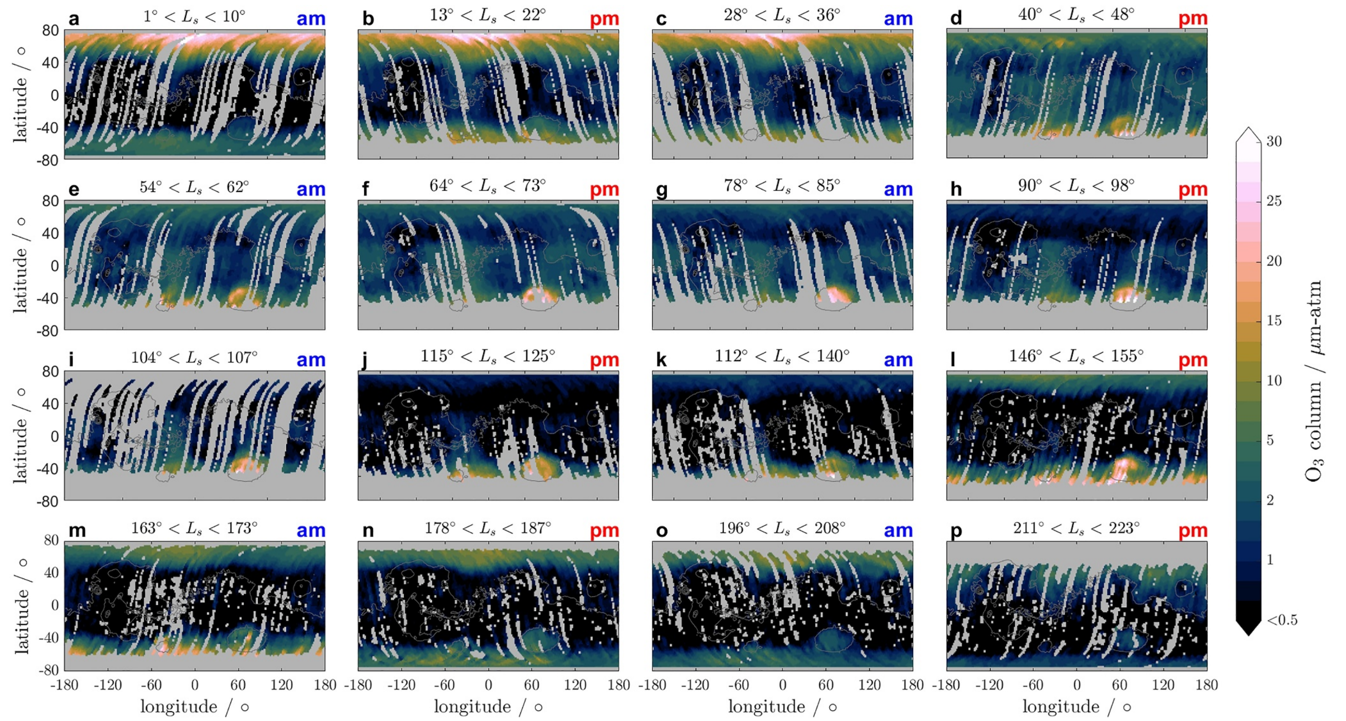

Figure 8. Same as Figure 7 but for the MY 36 from Ls = 0° through to $L_s = 223°$. Each panel alternates between the morning and afternoon atmosphere that is, panels (a, c, e, g, I, k, m, o), represent local solar times between 0600 LST and 1200 LST and panels (b, d, f, h, j, l, n, p) represent the afternoon retrievals from 1200 LST to 1800 LST. The lower coverage in the dataset in MY 36 compared to MY 35 is a result of the 50% duty cycle that was implemented to preserve the instrument life.

result in the observed increase in the O_3 column abundance with a stationary wave-1 or wave-2 pattern observed. At this time, the O_3 longitudinal variations are once again forced by perturbations in the polar vortex.

Low latitudes: The expected increase in low-latitude O_3 column abundances is observed at aphelion, beginning around $L_s = 25°$ and ending around $L_s = 160°$ in both MY 35 and MY 36. At this time, the observed column abundances in the low latitudes (Figures 7c–7j and 8b–8i) are typically between 1 and 4 µm-atm and exhibit a strong longitudinal dependence forced by topography in good agreement with previous studies (see Clancy et al., 2016; Lefèvre et al., 2004). Distinct enhancements are observed over the Argyre basin and extend over the Valles Marineris region. On the other hand, there is always less ozone over the Tharsis bulge, likely due to the altitude of the plateau.

In Figure 9, we show the correlation between O_3 and water ice for the period $L_S = 79°–90°$. The distribution of O_3 correlates well with the observed distribution of water ice clouds, with the region around and north of Valles Marineris exhibiting the highest O_3 abundances and the greatest extent of cloud cover. North of Hellas from 60°E and eastward to Tharsis also show higher cloud opacities and elevated O_3 columns. Similarly, in regions with low O_3 abundances we see reduced cloud coverage and opacities, for example, north eastward of Hellas and also above 30°N where we observed a mid-latitude zonal band centered at 40°N that has substantially less O_3 (typically <2 µm-atm); a region associated with lower water ice coverage and higher water vapor concentrations (Crismani et al., 2021; Olsen et al., 2022). Coincident observations of O_3 and water vapor vertical profiles by TGO/ACS revealed that this region of reduced O_3 is associated with increased O_3 destruction in the lower atmosphere by an influx of water vapor from the sublimating north polar cap (Olsen et al., 2022). This increases the water vapor abundance below 20 km and hence the number of available HO_x species that destroy O_3.

The observed correlation between water ice and O_3 agrees with equatorial O_3 vertical profiles from the aphelion season which showed an O_3 layer roughly corresponding to just above the water ice layers between 30 and 40 km (Lebonnois et al., 2006; Olsen et al., 2022; Patel et al., 2021). Also, comparing the water ice distribution to the water vapor distribution presented Crismani et al. (2021) shows, perhaps not unexpectedly, an anti-correlation between the two species. These results could support evidence from the vertical O_3 profiles that a cold layer

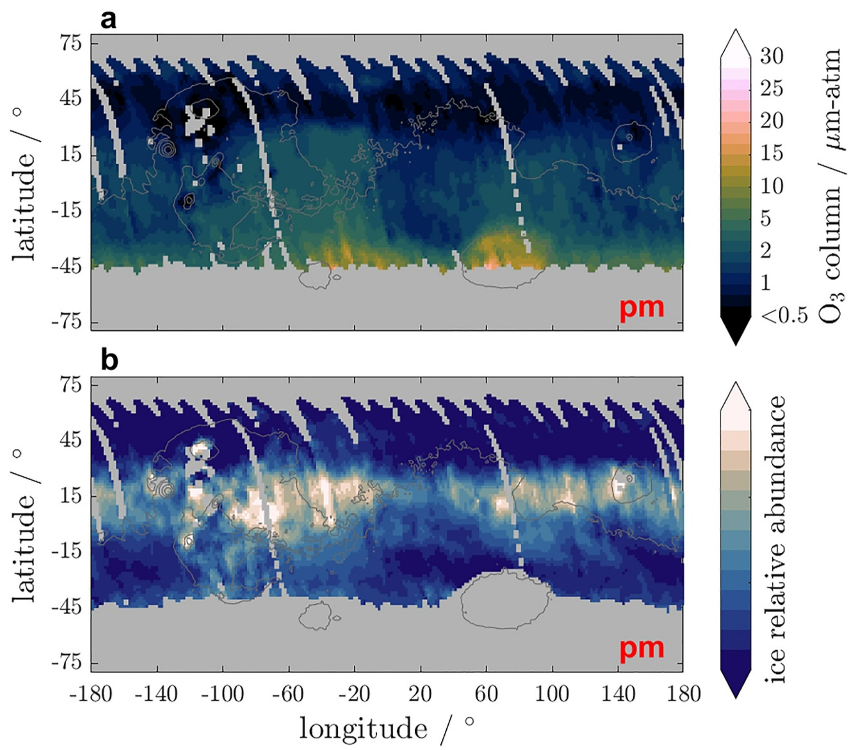

Figure 9. The geographical distribution of (a) O_3 normalized to a reference pressure of 610 pa and (b) water ice clouds for L_S = 79°–90°. Note that the color scale is non-linear in panel (a) to highlight lower O_3 columns.

exists that leads to water actively freezing out of the atmosphere and allowing ozone to build-up (Olsen et al., 2022).

The general seasonal behavior in the O_3 column abundances during aphelion measured by UVIS is consistent between MY 35 and MY 36. However, we see significant interannual variability between MY 35 and MY 36 within these seasonal trends. Figures 7c–7h and 8c–8h show the build-up of the aphelion O_3 enhancement in the MY 35 and MY 36, respectively. From these O_3 maps, we see that from early spring to the summer solstice, the O_3 column abundances in MY 35 seem to be diminished in comparison to MY 36. In Figure 10, we show a timeseries of the O_3 column abundances between 20°S and 20°N as a function L_S for the aphelion season in MY 35 and MY 36. In the lead up to the northern summer solstice, MY 35 consistently shows reduced O_3 column abundance compared to MY 36, with the average abundance being ~14% lower at low latitudes when Mars is at aphelion (L_S = 71°). Post aphelion, the O_3 trends in MY 35 and MY 36 re-converge. The key difference between MY 35 and MY 36 is that the MY 35 aphelion period followed an intense Global Dust Storm (GDS) in the preceding perihelion season in MY 34. Clancy et al. (2016) also reported reduced equatorial O_3 column abundances at the aphelion for MY29, which also followed a GDS in the preceding year (MY28). These new results from UVIS observations could provide further evidence suggesting that a GDS in the perihelion season can have a prolonged impact on the martian atmosphere, causing significant changes in both atmospheric and surface conditions leading to interannual variations in atmospheric photochemistry.

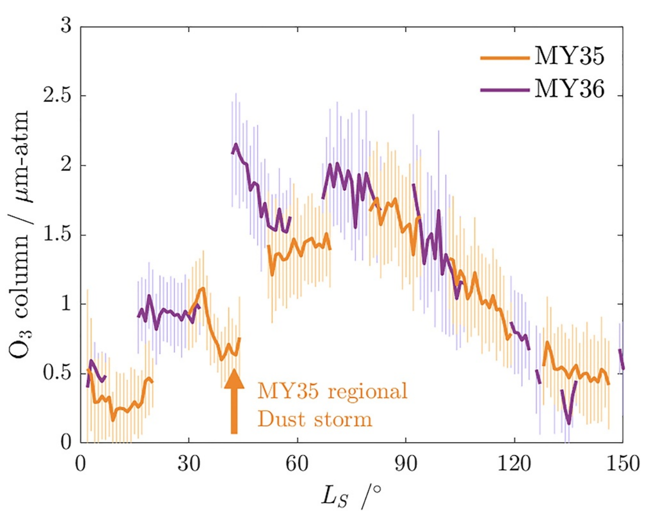

Figure 10. Averaged UVIS O_3 columns between 20°S and 20°N as a function of L_S for the aphelion season in MY 35 (orange line) and MY 36 (purple line). The vertical lines give the 1-σ dispersion of the data.

Another explanation for the reduced O_3 columns in MY 35 could be the early large-scale regional dust storm (A-storm) that occurred in the northern hemisphere in spring (between L_S = 30°–50°). This dust storm resulted in a significant increase in the atmospheric dust loading and led to elevated

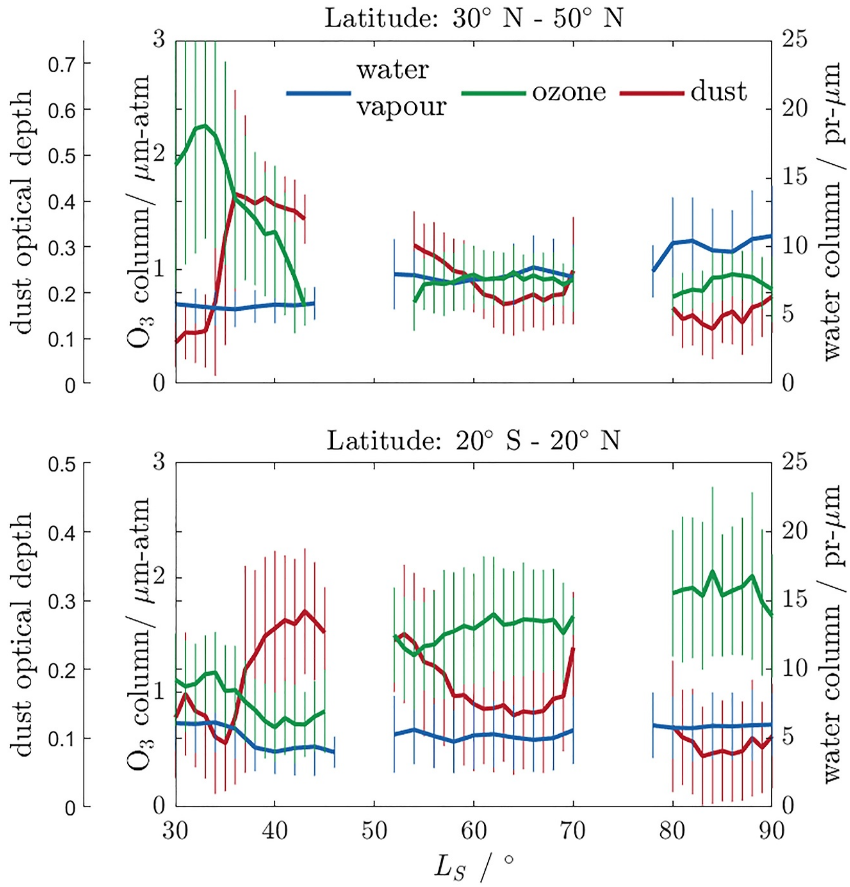

Figure 11. Evolution of the O_3 columns (green line), dust opacity (red line) by product from our retrieval and water vapor columns (blue line) from NOMAD (Crismani et al., 2021) in MY35 from $L_S = 30°–90°$ at (a) equatorial latitudes between −20°S and 20°N and (b) northern latitudes between 30°N and 50°N, where the regional dust storm developed. The vertical lines for the water columns give the 1-σ dispersion in the data.

atmospheric temperatures, with MCS reporting zonal mean temperatures that reached nearly 20 K above seasonal values in the northern hemisphere and 15 K in the southern hemisphere (Kass et al., 2022). The effect of the MY35 A-storm on the O_3 column was evidenced by a sharp reduction in O_3 starting at $L_S \sim 34°$. In the UVIS O_3 data, we see that this dust storm resulted in a significant reduction in the O_3 abundance at mid and equatorial latitudes (see Figure 7d), at a time when the O_3 abundance is expected to be gradually increasing. The decrease in O_3 also coincides with significantly reduced water ice cloud coverage as seen by MARCI (Kass et al., 2022) and suggests that the warmer atmospheric temperatures during the storm were sufficient to alter the water saturation conditions. In Figure 11, we show the evolution of the O_3 columns, the dust optical depth (by product of the retrieval) and the water vapor column measured by NOMAD (Crismani et al., 2021) in two latitude bands covering equatorial latitudes between −20°S and 20N (panel a) and northern latitudes between 30°N and 50°N (panel b), where the regional dust storm developed. The dust opacity begins to increase around $L_S = 34°$, coinciding with the observed decrease in the O_3 abundance. At equatorial latitudes, a peak in the dust opacity is seen at $L_S = 43°$, which coincides with the minima in observed O_3 abundance. Opposed to the behavior of dust, the water vapor abundance shows little change as a result of the A-storm at northern latitudes, with a gradual increase in the water abundance observed toward the northern summer solstice. At equatorial latitudes, the water abundance remains relatively constant; however, there is a potential decrease in the water abundance that begins at $L_S = 34°$ and coincides with the observed decrease in the O_3 abundance.

To explain the observed behavior in O_3 during the MY35 A-storm , we present, in Figure S3 in Supporting Information S1, a comparison of the temperature (panels a, b), dust (panels c, d), water vapor (panels e, f), and O_3 (panels g, h) vertical distributions in MY35 and MY36 between $L_s = 35°–55°$. As evident in Figure S3 in

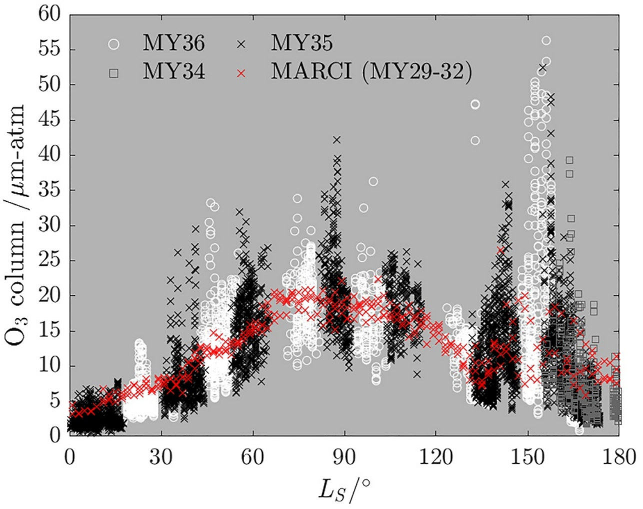

Figure 12. The O_3 column abundance measured by UVIS within the Hellas Basin in MY 34 (gray squares), MY 35(black crosses), and MY 36 (white circles) between $L_S = 0°–180°$. The red crosses show the MARCI O_3 columns within Hellas for MY29-3. The O_3 column abundances were averaged into 1° L_S bins in order to show the general trend of O_3 within Hellas. The boundary of Hellas was defined as an ellipse with a semi-major axis of ∼42°, a semi-minor axis of 22° and centered at latitude = 41.5°S and longitude = 69.6°.

Supporting Information S1, the A-storm resulted in vertically elevated temperatures in MY35, especially in the northern hemisphere. This increase in temperature is coupled to the observed increase in the atmospheric dust loading that extends to at least 30 km (see Figure S3c in Supporting Information S1). In Figures S3e and S3f in Supporting Information S1, the ACS water vapor profiles (Fedorova et al., 2023) show that the warmer temperatures resulted in an increase in the water vapor abundance in the middle atmosphere at northern latitudes in MY35. Increased water vapor is also seen in southern latitudes but to a lesser extent when compared to MY36. Unfavorable beta angles prevented measurement at equatorial latitudes. Compared to MY36, MY35 shows reduced O_3 abundances between 20–50 km across most latitudes (with the exception of south polar latitudes) during the MY35 A-storm (Figures S3g and S3h in Supporting Information S1). We associate this reduction in O_3 with the increase in water at these altitudes and is characteristic of the anti-correlation between the two species. While it does not appear the MY35 A-storm caused an increase in the total amount of water vapor in the atmosphere, as evidence by the total water column measured by NOMAD, the increased dust loading and the subsequent warming of the atmosphere did result in the redistribution of the available water vapor (and by association, HO_x) to higher altitudes which resulted in the destruction of O_3 above 20 km which could explain the lower O_3 columns observed by the UVIS nadir channel.

While we have shown that the regional A-storm in MY35 resulted in lower O_3 columns between $L_S = 30°–60°$, it is not possible, with currently available published data, to determine if the reduced O_3 columns beyond $L_S = 60°$ in MY 35 is a result of the regional storm, a lingering effect of the MY 34 dust storm or both.

High southern latitudes: The O_3 distribution at high latitudes in the southern hemisphere follows a similar trend to that in the northern hemisphere. The largest O_3 abundances are seen around the weakly sunlit edges of the polar night during late autumn, winter, and spring ($L_S = 20°–160°$), with typical abundances of above 20 μm-atm. During this time, the O_3 column abundances show a distinct longitudinal dependence associated with O_3 increases in the deep basins of Hellas and Argyre. To investigate O_3 column abundance variations within Hellas, we computed the temporal variability of the O_3 column abundances within the Hellas basin, whose boundary was defined as an ellipse with a semi-major axis of 43.5° and a semi-minor axis of 23° centered at 41°S and 69.6°E. The O_3 columns within Hellas for both UVIS and MARCI are averaged into 1° L_S bins and compared in Figure 12. We generally observe a gradual increase in the O_3 columns beginning near $L_S \sim 25°$ and peaking around $L_S = 87°$ in MY 35 and $L_S = 74°$ in MY 36. The observed peak in MY 35 is later in the season than that observed by MARCI ($L_S \sim 70°$); however, we see reasonable agreement in MY 36 with the MARCI observations. The variability in the timing of the second O_3 peak within the Hellas basin could be due to interannual variability, as reported by Clancy et al. (2016). However, UVIS had poor coverage of the Hellas Basin between $L_S = 66°–71°$ in MY 35, and therefore, we cannot say if a peak near $L_S = 70°$ (more consistent with MARCI) was present. A second peak in the Hellas O_3 column abundance in both MY 35 and MY 36 is seen between $L_S = 140°–160°$, with the tail-end observed in MY 34, in good agreement with the MARCI observations. In terms of absolute abundances within Hellas Basin, the largest column abundances are seen at the time of the second peak, where O_3 abundances frequently exceeded 30 μm-atm.

Perihelion season: Increased solar insolation during southern summer leads to a warmer, wetter, and more active atmosphere resulting in the O_3 column abundances at equatorial and southern latitudes being significantly reduced typically below the detection limit of UVIS (∼0.7 μm-atm). Larger O_3 abundances are observed around the edge of the northern polar region with higher abundances expected toward the pole (Clancy et al., 2016). Such polar observations by UVIS, however, are prevented by the on-set of the polar night and the 74° inclined TGO orbit.

As discussed in Section 5.1, high dust loading conditions can result in O_3 artifacts in the data, usually around the perihelion, and are particularly noticeable in MY 34 during the GDS and to a lesser extent in MY 35 and MY 36.

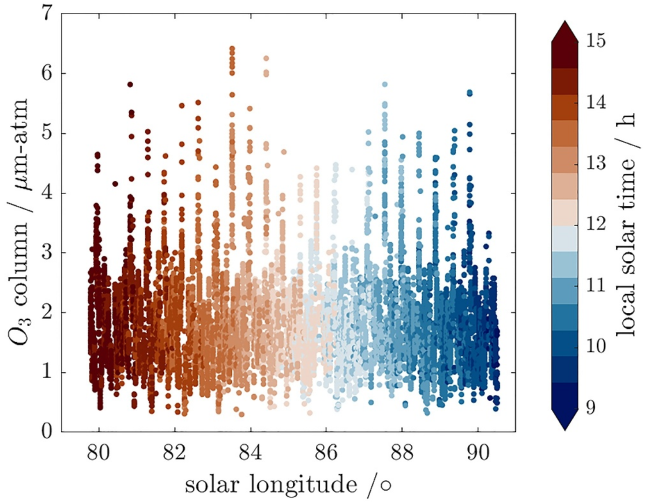

Figure 13. The retrieved UVIS O_3 columns in MY35 between 15°S and 75°N at all longitudes as a function of L_S and LST (shown in color) for the period L_S = 79.5–90.5°.

The contamination is likely due to changes in the atmospheric dust microphysical properties during high dust loading events, namely the particle size distribution as a function of altitude. Sky brightness measurements taken by the Curiosity Rover during the MY 34 GDS were analyzed by Lemmon et al. (2019), who showed that the dust particle size rapidly increased to >3 μm in Gale Crater, which is significantly larger than the value of 1.8 μm used in these retrievals. Analyzing a set of high dust loading cases, we also found a strong correlation between dust artifacts and the dust ceiling altitude, whereby the higher the altitude of dust aerosol, the more strongly suppressed the Rayleigh scattering inflection is below 260 nm. An underprediction of the dust vertical extent resulted in an excess of Rayleigh scattering in our forward model, which was compensated for in the retrieval by an unphysical increase in the abundance of O_3.

5.2. Diurnal Variations

A key advantage of UVIS nadir observations is the measurement of O_3 at different LSTs. However, understanding the diurnal ozone cycle from the UVIS dataset requires de-coupling from any seasonal or geographic variations as well as from the potentially false detections resulting from the high dust loading conditions. Given these criteria, we restrict our analysis to the aphelion season and avoid high southern latitudes where we observe strong longitudinal (see Figures 7 and 14c). Strong longitudinal variation in the O_3 column abundance from perturbations in the polar vortex and the formation/decay of the equatorial O_3 aphelion enhancement exclude the spring/autumn season. These limitations leave a short period around the summer solstice (L_S = 79.5°–90.5°) to examine potential diurnal variations with high confidence. In Figure 13, we show the UVIS O_3 columns between 15°S and 75°N at all longitudes against L_S and LST (shown in color). This period spans the peak of the equatorial O_3 band, and in the UVIS data, we see no obvious seasonal trends and good LST coverage spanning early morning (∼09 LST) to mid-afternoon (∼15 LST) is observed.

In our selected L_S period, the morning (<1200 LST) and afternoon (>1200 LST) O_3 columns were binned into 1.5° latitude and longitude bins to create O_3 maps of the morning and afternoon atmosphere (equivalent to those in Figures 7 and 8), as shown in Figures 14a and 14b respectively. The difference between the morning and afternoon O_3 column abundances is given in Figure 14c. The O_3 column abundances show regional differences in the diurnal behavior. For example, the northern mid-latitude band of lower O_3 centered at 45°N tends to show higher O_3 column abundances in the morning, especially in a region North of Tharsis (see Region 1 in Figure 11). The Tharsis ridge also tends to show higher O_3 column abundances in the morning, except around the volcanoes where we observe higher O_3 abundances in the afternoon. Wolff et al. (2022) showed that water ice clouds over Tharsis evaporate throughout the day but tend to remain around the Tharsis volcanoes. Therefore, the increase in afternoon O_3 near the volcanoes could be linked to an O_3 layer above the persistent cloud cover. We also observe higher morning O_3 column abundances in an equatorial region between 0°E to 70°E; this region tends to be associated with regions of low O_3 column abundances (see Figures 7e–7h and 8e–8g), lower water ice coverage (see Figure 9) and of high water vapor column abundances (Crismani et al., 2021). Conversely, regions where we observed higher equatorial O_3 and water ice abundances (Figure 9), particularly north of the Argyre Basin and extending northwards to the Valles Marineris and, to a lesser extent, from 70°E to 175°W between −15°S and 20°N show greater O_3 column abundances in the afternoon. At latitudes >30°S in the southern hemisphere, we see significant variations in the O_3 diurnal cycle on small spatial scales and associate this to longitudinal, rather than diurnal, variations possibly caused by perturbations in the polar vortex.

As illustrated in Figure 14, we investigate four regions: Region 1 (outlined by the solid line) and Region 3 (dashed box) are regions that exhibit higher O_3 column abundances in the morning, while Region 2 (dotted box) and Region 4 (outlined by dash-dot line) are those which show greater afternoon O_3 column abundances. In Figures 15a–15d, we show the retrieved O_3 column abundances in each region as a function of LST and L_S (color) and show the averaged UVIS O_3 column abundances to emphasize the diurnal trends in each region. The averaged UVIS O_3 column abundances are compared against modeled O_3 from the latest OpenMars database (version 4), which contains the water vapor reanalysis dataset (Holmes et al., 2024). This updated OpenMarsv4 reanalysis

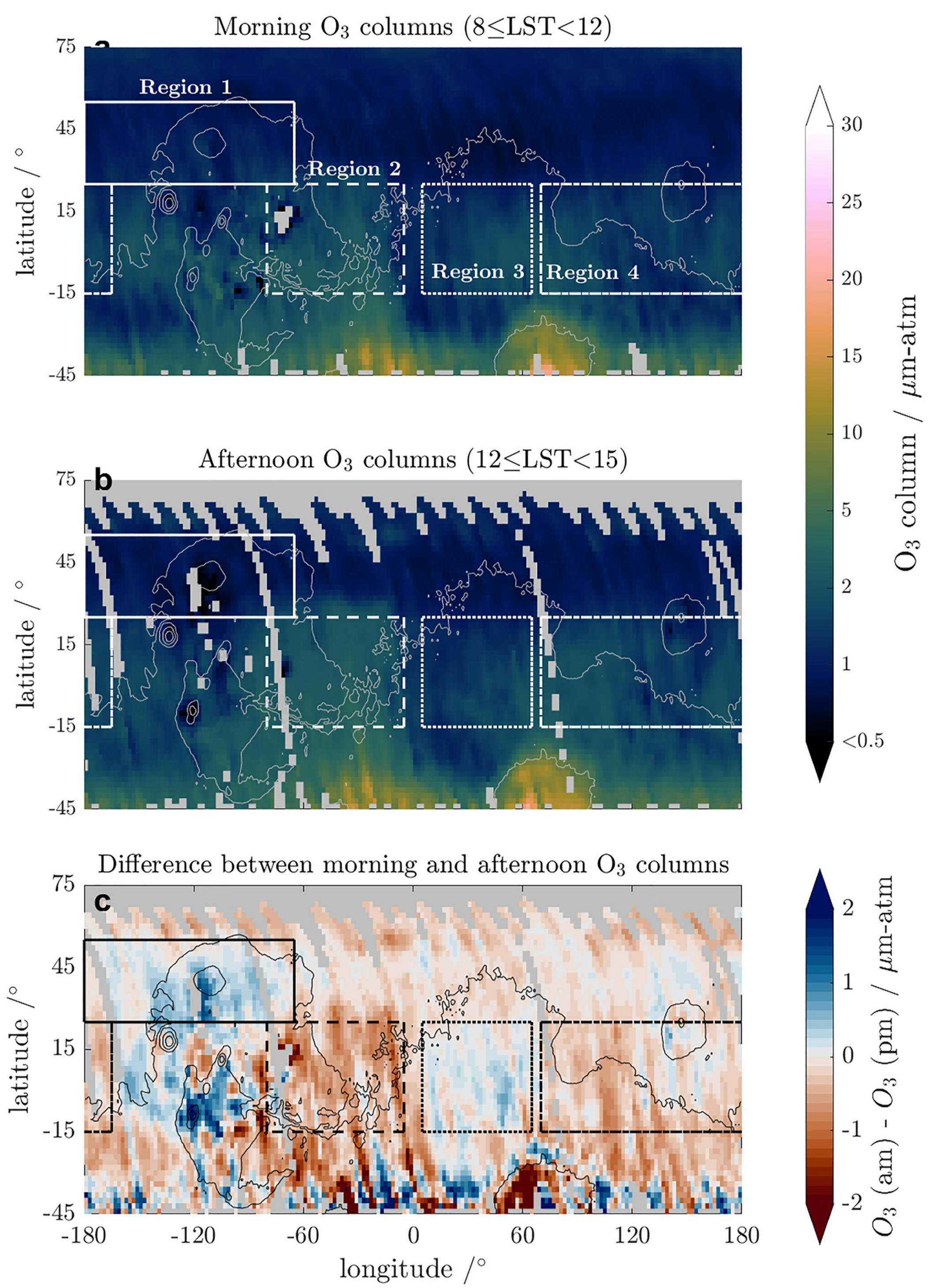

Figure 14. The UVIS O_3 column abundances as a function of latitude and longitude between $L_S = 79.5$–90.5 in MY 35 for (a) The morning between $8 \leq$ LST < 12LST and (b) the afternoon $12 \leq$ LST <15. (c) The difference between the morning and afternoon O_3 column abundances (am–pm). The four different regions investigated are outlined in (c) by a solid line (Region 1), dash line (Region 2), dotted line (Region 3), and dash-dot line (Region 4).

dataset differs from the OpenMarsv1 dataset used to generate our reference atmosphere since, as well as assimilating MCS dust column abundances and temperatures (Kleinböhl et al., 2017), it also includes the assimilation of water vapor column abundances and vertical profiles from NOMAD (Aoki et al., 2019; Crismani

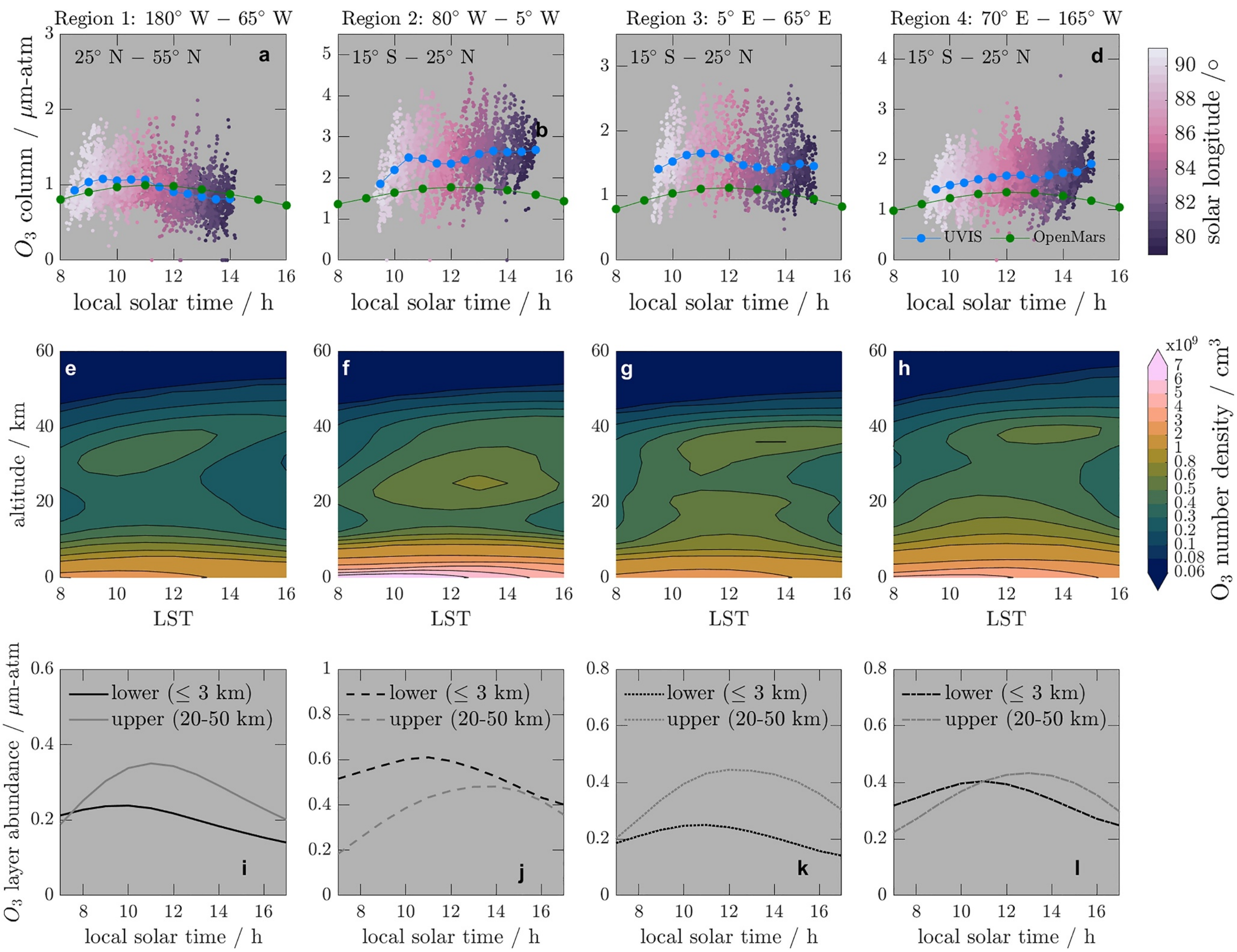

Figure 15. The top row shows the measured O_3 column abundances as a function of L_S (color) and LST for (a) Region 1, (b) Region 2, (c) Region 3, (d) Region 4. The UVIS O_3 column abundances are binned into half-hour LST bins to show the diurnal trends (blue line) and compared against the OpenMARS (water vapor reanalysis) dataset (Holmes et al., 2024) (green line). The middle row (e-h) shows the simulated vertical profile of O_3 as a function of altitude and LST (color) for the four Regions. Finally, the bottom row of figures (i–l) shows the vertical integrated layer abundance for the near surface O_3 layer (<3 km) and the upper O_3 layer (20–50 km).

et al., 2021; Villanueva et al., 2021) and ACS (Alday et al., 2021; Fedorova et al., 2023) into the latest version of the PCM UK-spectral that includes the chemical scheme from Lefèvre et al. (2021). As such, this dataset represents the most accurate model of Mars O_3 since the water vapor distribution is well constrained by observations where possible.

In general, the observed mean dayside diurnal variations in the O_3 column abundance in the four regions is relatively small (typically less than 1.0 μm-atm), which agrees with modeling results that show diurnal variations during the day are small compared to the day/night differences (Lefèvre et al., 2004). However, we do see some consistent trends in the diurnal profiles. For example, in Region 1 and Region 3, a peak in the O_3 abundance is seen between 0900 LST and 1100 LST, followed by a gradual decline in the O_3 abundance after the mid-morning peak toward the afternoon. This mid-morning peak agrees well with model simulations by Lefèvre et al. (2004), who showed that the photolysis of NO_2 in the lowest 3 km can result in a morning peak of O_3. Compared to Region 1, a potential weak secondary peak in the mid-afternoon is observed in Region 3 near 1430 LST. A mid-morning peak is also observed in Region 3; however, the profile is superimposed on an underlying O_3 column abundance that steadily increases from early morning through to mid-afternoon. Finally, in Region 4, the O_3 column abundance steadily increases from morning to mid-afternoon with no observed peaks. These profiles show more structure and, in some cases (Region 2 and Region 4), considerably different to the OpenMarsv4 O_3

10.1029/2023JE008270

diurnal cycle, which tends to show a consistent profile in all regions, that is, an increasing O_3 column abundance toward a late-morning or noon peak and a subsequent decrease in the afternoon.

As previously mentioned, in northern summer O_3 is expected to form in two layers, one below and another above the hygropause. This two-layer structure is reproduced well in the OpenMarsv4 dataset, as illustrated in Figures 15e and 15f, which shows the vertical distribution of O_3 as a function of LST in our four regions. In the OpenMarsv4 reanalysis dataset, the increase in the lower layer is associated with NO_2 and shows a higher O_3 abundance in the morning, whereas the upper layer is associated with H_2O (or rather forms due to the absence of water since it condenses into clouds) and shows higher O_3 abundances in the afternoon. These two layers are therefore different in origin, and indeed the layers show an opposite diurnal trend. The difference in the diurnal profiles of the two layers is emphasized in Figures 15i–15l which shows the integrated abundance in the lower and upper layer as a function of LST. The similarity between the UVIS O_3 diurnal profile and the near surface layer from OpenMarsv4 suggests that the observed diurnal cycle in Region 1 and Region 3 is driven by diurnal changes in the lower O_3 layer. Similarly, the increase in O_3 in the upper layer from morning to afternoon could explain the gradual increase we observe in the O_3 columns in Region 2 and Region 4 as well as the early afternoon increase in the O_3 abundance in Region 3.

The different O_3 diurnal trends between UVIS and OpenMarsv4 could be due to the opposing contribution of these two layers that may not be well represented in the model. In particular, the UVIS measurements in Region 3 and Region 4 suggest that the upper layer has a larger contribution than predicted from the model, whereas Region 1 suggests a weaker upper layer than predicted. The under/overprediction in the amount of O_3 in the upper layer in the model could also be due to the under/overestimation of water ice cloud condensation, which directly impacts the density of water vapor and HO_x in the atmosphere.

Another potential interpretation for the underestimation of ozone in the upper layer is heterogeneous chemistry (Brown et al., 2022; Lefèvre et al., 2008). Currently, heterogeneous processes are included in the PCM-UK Spectral model and follow the formulation of Lefèvre et al. (2008). Brown et al. (2022) investigated a more detailed heterogeneous chemistry scheme using a 1-D model and found a positive vertical correlation between ozone and water ice when the water vapor abundance was low. However, this new heterogeneous formulation has not yet been fed back into 3-D simulations.

6. Conclusions

As a highly reactive gas, O_3 plays a key role in Mars photochemistry and measurement of its distribution can provide information on the variations of H_2O and also the hard to detect HO_x species. Accurate O_3 measurements can also be used to validate and refine global climate models to improve our understanding of the Mars atmosphere.

We presented the O_3 distribution retrieved from UVIS measurements in MY 34 ($L_S = 150°$) through to the end of MY 36, demonstrating that robust measurement of Mars O_3 can be obtained from the UVIS nadir measurements showing good agreement with MARCI O_3 columns with no systematic offset that would be indicative of residual straylight effects.

The O_3 climatology for MY 34–MY 36 shows the expected general spatio-temporal distribution, with higher O_3 column abundances in the spring, autumn and winter poles, the build-up of O_3 at low latitudes during aphelion, and low O_3 column abundances during the warmer perihelion season. A correlation between the formation and distribution of aphelion O_3 enhancement and water ice was observed at mid and equatorial latitudes in the northern spring and summer. This correlation follows evidence in the observed aphelion O_3 vertical profiles that found an O_3 layer just above the water ice clouds. The build-up of O_3 in the Hellas basin is also observed starting at $L_S = 25°$ through to 100° with a peak in O_3 abundances in MY 35 occurring slightly later in the season ($L_S = 87°$) compared to MARCI observations (Clancy et al., 2016). However, as indicated, this could be a result of insufficient coverage by UVIS over $L_S = 66°–71°$.

The equatorial O_3 column abundances during the northern summer solstice in MY 35 between $L_S = 60°–85°$ were observed to be ∼14% lower compared to MY 36. MY 35 experienced an early larger scale regional dust storm, which we have shown resulted in the near global reduction in both O_3 and water ice between $L_S \sim 40°–50°$. Another key difference between the two years was that the MY 35 aphelion season directly followed a GDS in MY 34, and as evidenced by MARCI, lower O_3 columns were observed in the aphelion season of MY 29 following the MY 28 GDS. While the UVIS data alone is insufficient to determine the main driver that resulted in the lower O_3 columns in MY 35, these results could provide further evidence of a correlation between reduced O_3 abundances at aphelion and the occurrence of a GDS in the preceding perihelion season, further highlighting the importance of GDS in the present-day climate in causing interannual variations in trace gases beyond the year of the event itself.

The UVIS O_3 column abundances show that dayside diurnal variations are generally small (<1.5 μm-atm) and show differing behavior in different regions on the planet, dependent on the relative abundance of O_3 in the near-surface or upper O_3 layer. Regions with low O_3 abundance, and generally associated with larger water vapor columns and a thin upper O_3 layer, exhibited a mid-morning peak in O_3 and a subsequent decay in the O_3 column abundances in the afternoon. This is consistent with diurnal variations seen in the near-surface layer of the OpenMarsv4 assimilation dataset and agrees well with previous modeling results by Lefèvre et al. (2004), suggesting that the observed diurnal variations are driven by the photolysis of NO_2 in the early morning. Similarly, regions that exhibited higher O_3 column abundances show a gradual increase in the O_3 column abundances from morning to afternoon, consistent with diurnal variations shown by OpenMarsv4 in the upper O_3 layer. The UVIS measurements suggest that the upper O_3 layer plays a larger role in the daily variations of O_3 than is currently predicted and could point toward an under/overestimation of water ice condensation or heterogeneous processes.

Data Availability Statement

Public access to all ExoMars TGO data is available through the ESA Planetary Science Archive (archives.esac.esa.int/psa/). Instruction on how to find NOMAD data within the PSA is available on the NOMAD website (https://nomad.aeronomie.be/index.php/data-psa-users). The NOMAD website also provides useful details about the NOMAD data and how to use it. The OpenMARS database can be downloaded from Holmes et al. (2022a) and the water reanalysis dataset from Holmes et al. (2024). The DISORT radiative transfer code is available from the LLLab DISORT Website, http://www.rtatmocn.com/disort/. The data products derived from the UVIS measurements in this study can be downloaded from The Open University data repository (Mason & Patel, 2023).

Acknowledgments
The NOMAD experiment is led by the Royal Belgian Institute for Space Aeronomy (IASB-BIRA), with Co-PI teams in the United Kingdom (Open University), Spain (IAA-CSIC) and Italy (INAF-IAPS). This work was enabled through UK Space Agency Grants ST/V002295/1, ST/V005332/1, ST/X006549/1, ST/Y000234/1 and ST/R003025/1, ST/Y000196/1 and the Science and Technology Facilities Council funding through Grant ST/X001180/1. This project acknowledges funding by the Belgian Science Policy Office (BELSPO), with the financial and contractual coordination by the ESA Prodex Office (PEA 4000103401, 4000121493), by Spanish Ministry of Science and Innovation (MCIU) and by European funds under Grants PGC2018-101836-B-I00 and ESP2017-87143-R (MINECO/FEDER), as well as by the Italian Space Agency through Grant 2018-2-HH.0. This work was supported by the Belgian Fonds de la Recherche Scientifique—FNRS under Grant 30442502 (ET_HOME). The IAA/CSIC team acknowledges financial support from the State Agency for Research of the Spanish MCIU through the "Center of Excellence Severo Ochoa" award for the Instituto de Astrofísica de Andalucía (SEV-2017-0709). US investigators were supported by the National Aeronautics and Space Administration.

References

Abramov, O., & McEwen, A. (2004). An evaluation of interpolation methods for Mars Orbiter Laser Altimeter (MOLA) data. *International Journal of Remote Sensing*, *25*(3), 669–676. https://doi.org/10.1080/01431160310001599006

Acton, C., Bachman, N., Semenov, B., & Wright, E. (2018). A look towards the future in the handling of space science mission geometry. *Planetary and Space Science*, *150*, 9–12. https://doi.org/10.1016/j.pss.2017.02.013

Acton, C. H., Jr. (1996). Ancillary data services of NASA's navigation and ancillary information facility. *Planetary and Space Science*, *44*(1), 65–70. https://doi.org/10.1016/0032-0633(95)00107-7

Alday, J., Trokhimovskiy, A., Irwin, P. G. J., Wilson, C. F., Montmessin, F., Lefèvre, F., et al. (2021). Isotopic fractionation of water and its photolytic products in the atmosphere of Mars. *Nature Astronomy*, *5*(9), 943–950. https://doi.org/10.1038/s41550-021-01389-x

Aoki, S., Vandaele, A. C., Daerden, F., Villanueva, G. L., Liuzzi, G., Clancy, R. T., et al. (2022). Global vertical distribution of water vapor on Mars: Results from 3.5 years of ExoMars-TGO/NOMAD science operations. *Journal of Geophysical Research: Planets*, *127*(9), e2022JE007231. https://doi.org/10.1029/2022je007231

Aoki, S., Vandaele, A. C., Daerden, F., Villanueva, G. L., Liuzzi, G., Thomas, I. R., et al. (2019). Water vapor vertical profiles on Mars in dust storms observed by TGO/NOMAD. *Journal of Geophysical Research: Planets*, *124*(12), 3482–3497. https://doi.org/10.1029/2019je006109

Barth, C. A., Hord, C. W., Stewart, A. I., Lane, A. L., Dick, M. L., & Anderson, G. P. (1973). Mariner 9 ultraviolet spectrometer experiment: Seasonal variation of ozone on Mars. *Science*, *179*(4075), 795–796. https://doi.org/10.1126/science.179.4075.795

Bell, J. F., III., Wolff, M. J., Malin, M. C., Calvin, W. M., Cantor, B. A., Caplinger, M. A., et al. (2009). Mars reconnaissance orbiter Mars color imager (MARCI): Instrument description, calibration, and performance. *Journal of Geophysical Research*, *114*(E8). https://doi.org/10.1029/2008je003315

Bertaux, J. L., Fonteyn, D., Korablev, O., Chassefre, E., Dimarellis, E., Dubois, J. P., & Stern, A. (2004). SPICAM: Studying the global structure and composition of the Martian atmosphere. In A. Wilson & A. Chicarro (Eds.), *Mars express: The scientific payload* (Vol. 1240, pp. 95–120). ESA SP-1240. ESA Publications Division.

Braude, A. S. M., Schneider, F., Gupta, N. M., Jain, S., Lefèvre, S. K., Curry, S. M., et al. (2023). Seasonal, latitudinal, and longitudinal trends in night-time ozone vertical structure on Mars from MAVEN/IUVS stellar occultations. *Journal of Geophysical Research: Planets*, *128*(5), e2022JE007697. https://doi.org/10.1029/2022je007697

Brown, M. A., Patel, M. R., Lewis, S. R., Holmes, J. A., Sellers, G. J., Streeter, P. M., et al. (2022). Impacts of heterogeneous chemistry on vertical profiles of Martian ozone. *Journal of Geophysical Research: Planets*, *127*(11), e2022JE007346. https://doi.org/10.1029/2022je007346

Clancy, R. T., Grossman, A. W., Wolff, M. J., James, P. B., Rudy, D. J., Billawala, Y. N., et al. (1996). Water vapor saturation at low altitudes around Mars aphelion: A key to Mars climate? *Icarus*, *122*(1), 36–62. https://doi.org/10.1006/icar.1996.0108

Clancy, R. T., & Nair, H. (1996). Annual (perihelion-aphelion) cycles in the photochemical behavior of the global Mars atmosphere. *Journal of Geophysical Research*, *101*(E5), 12785–12790. https://doi.org/10.1029/96je00836

Clancy, R. T., Smith, M. D., Lefèvre, F., McConnochie, T. H., Sandor, B. J., Wolff, M. J., et al. (2017). Vertical profiles of Mars 1.27 μm O_2 dayglow from MRO CRISM limb spectra: Seasonal/global behaviors, comparisons to LMDGCM simulations, and a global definition for Mars water vapor profiles. *Icarus*, *293*, 132–156. https://doi.org/10.1016/j.icarus.2017.04.011

Clancy, R. T., Wolff, M. J., Lefèvre, F., Cantor, B. A., Malin, M. C., & Smith, M. D. (2016). Daily global mapping of Mars ozone column abundances with MARCI UV band imaging. *Icarus*, *266*, 112–133. https://doi.org/10.1016/j.icarus.2015.11.016

Coddington, O. M., Richard, E. C., Harber, D., Pilewskie, P., Woods, T. N., Snow, M., et al. (2023). Version 2 of the TSIS-1 Hybrid solar reference spectrum and extension to the full spectrum. *Earth and Space Science*, *10*(3), e2022EA002637. https://doi.org/10.1029/2022EA002637

Connour, K., Wolff, M. J., Schneider, N. M., Deighan, J., Lefèvre, F., & Jain, S. K. (2022). Another one derives the dust: Ultraviolet dust aerosol properties retrieved from MAVEN/IUVS data. *Icarus*, *387*, 115177. https://doi.org/10.1016/j.icarus.2022.115177

Crismani, M. M. J., Villanueva, G. L., Liuzzi, G., Smith, M. D., Knutsen, E. W., Daerden, F., et al. (2021). A global and seasonal perspective of Martian water vapor from ExoMars/NOMAD. *Journal of Geophysical Research: Planets*, *126*(11), e2021JE006878. https://doi.org/10.1029/2021je006878

Daerden, F., Neary, L., Viscardy, S., Muñoz, A. G., Clancy, R. T., Smith, M. D., & Fedorova, A. (2019). Mars atmospheric chemistry simulations with the GEM-Mars general circulation model. *Icarus*, *326*, 197–224. https://doi.org/10.1016/j.icarus.2019.02.030

Daerden, F., Neary, L., Wolff, M. J., Clancy, R. T., Lefèvre, F., Whiteway, J. A., et al. (2022). Planet-wide ozone destruction in the middle atmosphere on Mars during global dust storm. *Geophysical Research Letters*, *49*(11), e2022GL098821. https://doi.org/10.1029/2022gl098821

Fedorova, A., Korablev, O., Perrier, S., Bertaux, J. L., Lefèvre, F., & Rodin, A. (2006). Observation of O_2 1.27 μm dayglow by SPICAM IR: Seasonal distribution for the first Martian year of Mars Express. *Journal of Geophysical Research*, *111*(E9). https://doi.org/10.1029/2006je002694

Fedorova, A., Montmessin, F., Trokhimovskiy, A., Luginin, M., Korablev, O., Alday, J., et al. (2023). A two-Martian years survey of the water vapor saturation state on Mars based on ACS NIR/TGO occultations. *Journal of Geophysical Research: Planets*, *128*(1), e2022JE007348. https://doi.org/10.1029/2022je007348

Fedorova, A., Trokhimovskiy, A., Lefèvre, F., Olsen, K. S., Korablev, O., Montmessin, F., et al. (2022). Climatology of the CO vertical distribution on Mars based on ACS TGO measurements. *Journal of Geophysical Research: Planets*, *127*(9), e2022JE007195. https://doi.org/10.1029/2022je007195

Fedorova, A. A., Montmessin, F., Korablev, O., Luginin, M., Trokhimovskiy, A., Belyaev, D. A., et al. (2020). Stormy water on Mars: The distribution and saturation of atmospheric water during the dusty season. *Science*, *367*(6475), 297–300. https://doi.org/10.1126/science.aay9522

Forget, F., Hourdin, F., Fournier, R., Hourdin, C., Talagrand, O., Collins, M., et al. (1999). Improved general circulation models of the Martian atmosphere from the surface to above 80 km. *Journal of Geophysical Research*, *104*(E10), 24155–24175. https://doi.org/10.1029/1999je001025

Giuranna, M., Wolkenberg, P., Grassi, D., Aronica, A., Aoki, S., Scaccabarozzi, D., & Formisano, V. (2021). The current weather and climate of Mars: 12 years of atmospheric monitoring by the Planetary Fourier Spectrometer on Mars Express. *Icarus*, *353*, 113406. https://doi.org/10.1016/j.icarus.2019.113406

Gröller, H., Montmessin, F., Yelle, R. V., Lefèvre, F., Forget, F., Schneider, N. M., et al. (2018). MAVEN/IUVS stellar occultation measurements of Mars atmospheric structure and composition. *Journal of Geophysical Research: Planets*, *123*(6), 1449–1483. https://doi.org/10.1029/2017je005466

Guha, B. K., Panda, J., & Wu, Z. (2021). Observation of aphelion cloud belt over Martian tropics, its evolution, and associated dust distribution from MCS data. *Advances in Space Research*, *67*(4), 1392–1411. https://doi.org/10.1016/j.asr.2020.11.010

Guslyakova, S., Fedorova, A., Lefèvre, F., Korablev, O., Montmessin, F., Trokhimovskiy, A., & Bertaux, J. L. (2016). Long-term nadir observations of the O_2 dayglow by SPICAM IR. *Planetary and Space Science*, *122*, 1–12. https://doi.org/10.1016/j.pss.2015.12.006

Hartley, W. N. (1881). X.—On the absorption spectrum of ozone. *Journal of the Chemical Society Transactions*, *39*(0), 57–60. https://doi.org/10.1039/ct8813900057

Holmes, J. A., Lewis, S. R., & Patel, M. R. (2017). On the link between Martian total ozone and potential vorticity. *Icarus*, *282*, 104–117. https://doi.org/10.1016/j.icarus.2016.10.004

Holmes, J. A., Lewis, S. R., & Patel, M. R. (2020). OpenMARS: A global record of Martian weather from 1999 to 2015. *Planetary and Space Science*, *188*, 104962. https://doi.org/10.1016/j.pss.2020.104962

Holmes, J. A., Lewis, S. R., & Patel, M. R. (2022a). OpenMARS MY34-35 database [Dataset]. *The Open University*. https://doi.org/10.21954/ou.rd.20340999.v2

Holmes, J. A., Lewis, S. R., & Patel, M. R. (2024). OpenMARS MY34-35 database [Dataset]. *The Open University*. https://doi.org/10.21954/ou.rd.24981669

Holmes, J. A., Lewis, S. R., Patel, M. R., Alday, J., Aoki, S., Liuzzi, G., et al. (2022b). Global variations in water vapor and saturation state throughout the Mars Year 34 dusty season. *Journal of Geophysical Research: Planets*, *127*(10), e2022JE007203. https://doi.org/10.1029/2022je007203

Holmes, J. A., Lewis, S. R., Patel, M. R., & Lefèvre, F. (2018). A reanalysis of ozone on Mars from assimilation of SPICAM observations. *Icarus*, *302*, 308–318. https://doi.org/10.1016/j.icarus.2017.11.026

Mischna, M. A., Villar, G., Kass, D. M., Dutta, S., Rafkin, S., Tyler, D., et al. (2022). Pre-and post-entry, descent and landing assessment of the Martian atmosphere for the Mars 2020 rover. *The Planetary Science Journal*, *3*(6), 147. https://doi.org/10.3847/psj/ac7148

Kass, D. M., Kleinboehl, A., Shirley, J. H., Cantor, B. A., & Heavens, N. G. (2022). Observations of the Mars Year 35 E (early) large-scale regional dust event. In *Seventh International Workshop on the Mars Atmosphere: Modelling and bservations* (p. 2301).

Khayat, A. S., Smith, M. D., Wolff, M., DaerdenNeary, F. L., Patel, M. R., López-Moreno, J. J., et al. (2021). ExoMars TGO/NOMAD-UVIS vertical profiles of ozone: 2. The high-altitude layers of atmospheric ozone. *Journal of Geophysical Research: Planets*, *126*(11), e2021JE006834. https://doi.org/10.1029/2021je006834

Kleinböhl, A., Friedson, A. J., & Schofield, J. T. (2017). Two-dimensional radiative transfer for the retrieval of limb emission measurements in the Martian atmosphere. *Journal of Quantitative Spectroscopy and Radiative Transfer*, *187*, 511–522. https://doi.org/10.1016/j.jqsrt.2016.07.009

Korablev, O., Montmessin, F., Trokhimovskiy, A., Fedorova, A. A., Shakun, A. V., Grigoriev, A. V., et al. (2018). The Atmospheric Chemistry Suite (ACS) of three spectrometers for the ExoMars 2016 trace gas orbiter. *Space Science Reviews*, *214*, 1–62. https://doi.org/10.1007/s11214-017-0437-6

Lebonnois, S., Quémerais, E., Montmessin, F., Lefèvre, F., Perrier, S., Bertaux, J., & Forget, F. (2006). Vertical distribution of ozone on Mars as measured by SPICAM/Mars Express using stellar occultations. *Journal of Geophysical Research*, *111*(E9). https://doi.org/10.1029/2005je002643

Lefèvre, F., Bertaux, J. L., Clancy, R. T., Encrenaz, T., Fast, K., Forget, F., et al. (2008). Heterogeneous chemistry in the atmosphere of Mars. *Nature*, *454*(7207), 971–975. https://doi.org/10.1038/nature07116

Lefèvre, F., Lebonnois, S., Montmessin, F., & Forget, F. (2004). Three-dimensional modeling of ozone on Mars. *Journal of Geophysical Research*, *109*(E7). https://doi.org/10.1029/2004je002268

Lefèvre, F., Trokhimovskiy, A., Fedorova, A., Baggio, L., Lacombe, G., Määttänen, A., et al. (2021). Relationship between the ozone and water vapor columns on Mars as observed by SPICAM and calculated by a global climate model. *Journal of Geophysical Research: Planets*, *126*(4), e2021JE006838. https://doi.org/10.1029/2021je006838

Lemmon, M. T., Guzewich, S. D., McConnochie, T., de Vicente-Retortillo, A., Martínez, G., Smith, M. D., et al. (2019). Large dust aerosol sizes seen during the 2018 Martian global dust event by the Curiosity rover. *Geophysical Research Letters*, *46*(16), 9448–9456. https://doi.org/10.1029/2019gl084407

Lewis, S. R., Read, P. L., Conrath, B. J., Pearl, J. C., & Smith, M. D. (2007). Assimilation of thermal emission spectrometer atmospheric data during the Mars Global Surveyor aerobraking period. *Icarus*, *192*(2), 327–347. https://doi.org/10.1016/j.icarus.2007.08.009

Määttänen, A., Lefèvre, F., Verdier, L., Montmessin, F., Listowski, C., Guilbon, S., et al. (2022). Ozone vertical distribution in Mars years 27–30 from SPICAM/MEX UV occultations. *Icarus*, *387*, 115162. https://doi.org/10.1016/j.icarus.2022.115162

Määttänen, A., Listowski, C., Montmessin, F., Maltagliati, L., Reberac, A., Joly, L., et al. (2013). A complete climatology of the aerosol vertical distribution on Mars from MEx/SPICAM UV solar occultations. *Icarus*, *223*(2), 892–941. https://doi.org/10.1016/j.icarus.2012.12.001

Markwardt, C. B. (2009). Non-linear least squares fitting in IDL with MPFIT. *arXiv preprint arXiv:0902.2850*.

Marmo, F. F., Shardanand, & Warneck, P. (1965). Ozone distribution in the atmosphere of Mars. *Journal of Geophysical Research*, *70*(9), 2270–2272. https://doi.org/10.1029/jz070i009p02270

Mason, J., & Patel, M. (2023). UVIS ozone abundances for 2.5 Mars Years [Dataset]. *The Open University*. https://doi.org/10.21954/ou.rd.24877095.v1

Mason, J. P., Patel, M. R., Leese, M. R., Hathi, B. G., Willame, Y., Thomas, I. R., et al. (2022). Removal of straylight from ExoMars NOMAD-UVIS observations. *Planetary and Space Science*, *218*, 105432. https://doi.org/10.1016/j.pss.2022.105432

Mateshvili, N., Fussen, D., Vanhellemont, F., Bingen, C., Dodion, J., Montmessin, F., et al. (2007). Martian ice cloud distribution obtained from SPICAM nadir UV measurements. *Journal of Geophysical Research*, *112*(E7). https://doi.org/10.1029/2006je002827

McCleese, D. J., Schofield, J. T., Taylor, F. W., Calcutt, S. B., Foote, M. C., Kass, D. M., et al. (2007). Mars Climate Sounder: An investigation of thermal and water vapor structure, dust and condensate distributions in the atmosphere, and energy balance of the polar regions. *Journal of Geophysical Research*, *112*(E5). https://doi.org/10.1029/2006je002790

McClintock, W. E., Schneider, N. M., Holsclaw, G. M., Clarke, J. T., Hoskins, A. C., Stewart, I., et al. (2015). The imaging ultraviolet spectrograph (IUVS) for the MAVEN mission. *Space Science Reviews*, *195*(1–4), 75–124. https://doi.org/10.1007/s11214-014-0098-7

Mishchenko, M. I., Travis, L. D., & Lacis, A. A. (2002). *Scattering, absorption, and emission of light by small particles*. Cambridge University Press.

Modak, A., Sheel, V., & Montmessin, F. (2019). Retrieval of Martian ozone and dust from SPICAM spectrometer for MY27–MY28. *Journal of Earth System Science*, *128*(6), 144. https://doi.org/10.1007/s12040-019-1167-9

Montmessin, F., Korablev, O., Lefèvre, F., Bertaux, J. L., Fedorova, A., Trokhimovskiy, A., et al. (2017). SPICAM on Mars Express: A 10 year in-depth survey of the Martian atmosphere. *Icarus*, *297*, 195–216. https://doi.org/10.1016/j.icarus.2017.06.022

Montmessin, F., & Lefèvre, F. (2013). Transport-driven formation of a polar ozone layer on Mars. *Nature Geoscience*, *6*(11), 930–933. https://doi.org/10.1038/ngeo1957

Nair, H., Allen, M., Anbar, A. D., Yung, Y. L., & Clancy, R. T. (1994). A photochemical model of the Martian atmosphere. *Icarus*, *111*(1), 124–150. https://doi.org/10.1006/icar.1994.1137

Olsen, K. S., Fedorova, A. A., Trokhimovskiy, A., Montmessin, F., Lefèvre, F., Korablev, O., et al. (2022). Seasonal changes in the vertical structure of ozone in the Martian lower atmosphere and its relationship to water vapor. *Journal of Geophysical Research: Planets*, *127*(10), e2022JE007213. https://doi.org/10.1029/2022je007213

Olsen, K. S., Forget, F., Madeleine, J. B., Szantai, A., Audouard, J., Geminale, A., et al. (2021). Retrieval of the water ice column and physical properties of water-ice clouds in the Martian atmosphere using the OMEGA imaging spectrometer. *Icarus*, *353*, 113229. https://doi.org/10.1016/j.icarus.2019.03.006

Olsen, K. S., Lefèvre, F., Montmessin, F., Trokhimovskiy, A., Baggio, L., Fedorova, A., et al. (2020). First detection of ozone in the mid-infrared at Mars: Implications for methane detection. *Astronomy and Astrophysics*, *639*, A141. https://doi.org/10.1051/0004-6361/202038125

Patel, M. R., Antoine, P., Mason, J., Leese, M., Hathi, B., Stevens, A. H., et al. (2017). NOMAD spectrometer on the ExoMars trace gas orbiter mission: Part 2—Design, manufacturing, and testing of the ultraviolet and visible channel. *Applied Optics*, *56*(10), 2771–2782. https://doi.org/10.1364/ao.56.002771

Patel, M. R., Sellers, G., Mason, J. P., Holmes, J. A., Brown, M. A. J., Lewis, S. R., et al. (2021). ExoMars TGO/NOMAD-UVIS vertical profiles of ozone: 1. Seasonal variation and comparison to water. *Journal of Geophysical Research: Planets*, *126*(11), e2021JE006837. https://doi.org/10.1029/2021je006837

Pearl, J. C., Smith, M. D., Conrath, B. J., Bandfield, J. L., & Christensen, P. R. (2001). Observations of Martian ice clouds by the Mars global Surveyor thermal emission spectrometer: The first Martian year. *Journal of Geophysical Research*, *106*(E6), 12325–12338. https://doi.org/10.1029/1999je001233

Perrier, S., Bertaux, J. L., Lefèvre, F., Lebonnois, S., Korablev, O., Fedorova, A., et al. (2006). Global distribution of total ozone on Mars from SPICAM/MEX UV measurements. *Journal of Geophysical Research*, *111*(E9). https://doi.org/10.1029/2006je002681

Piccialli, A., Vandaele, A. C., Willame, Y., Määttänen, A., Trompet, L., Erwin, J. T., et al. (2023). Martian ozone observed by TGO/NOMAD-UVIS solar occultation: An inter-comparison of three retrieval methods. *Earth and Space Science*, *10*(2), e2022EA002429. https://doi.org/10.1029/2022ea002429

Shimazaki, T., & Shimizu, M. (1979). The seasonal variation of ozone density in the Martian atmosphere. *Journal of Geophysical Research*, *84*(A4), 1269–1276. https://doi.org/10.1029/ja084ia04p01269

Smith, D. E., Zuber, M. T., Frey, H. V., Garvin, J. B., Head, J. W., Muhleman, D. O., et al. (2001). Mars Orbiter Laser Altimeter: Experiment summary after the first year of global mapping of Mars. *Journal of Geophysical Research*, *106*(E10), 23689–23722. https://doi.org/10.1029/2000je001364

Smith, M. D. (2004). Interannual variability in TES atmospheric observations of Mars during 1999–2003. *Icarus*, *167*(1), 148–165. https://doi.org/10.1016/j.icarus.2003.09.010

Smith, M. D. (2009). THEMIS observations of Mars aerosol optical depth from 2002–2008. *Icarus*, *202*(2), 444–452. https://doi.org/10.1016/j.icarus.2009.03.027

Stamnes, K., Tsay, S. C., Wiscombe, W., & Laszlo, I. (2000). DISORT, a general-purpose Fortran program for discrete-ordinate-method radiative transfer in scattering and emitting layered media: Documentation of methodology.

Thomas, G. E., & Stamnes, K. (2002). *Radiative transfer in the atmosphere and ocean*. Cambridge University Press.

Vandaele, A. C., Lopez-Moreno, J. J., Patel, M. R., Bellucci, G., Daerden, F., Ristic, B., et al. (2018). NOMAD, an integrated suite of three spectrometers for the ExoMars trace gas mission: Technical description, science objectives and expected performance. *Space Science Reviews*, *214*(5), 1–47. https://doi.org/10.1007/s11214-018-0517-2

Villanueva, G. L., Liuzzi, G., Crismani, M. M., Aoki, S., Vandaele, A. C., Daerden, F., et al. (2021). Water heavily fractionated as it ascends on Mars as revealed by ExoMars/NOMAD. *Science Advances*, *7*(7), eabc8843. https://doi.org/10.1126/sciadv.abc8843

Willame, Y., Depiesse, C., Mason, J. P., Thomas, I. R., Patel, M. R., Hathi, B., et al. (2022). Calibration of the NOMAD-UVIS data. *Planetary and Space Science*, *218*, 105504. https://doi.org/10.1016/j.pss.2022.105504

Willame, Y., Vandaele, A. C., Depiesse, C., Lefèvre, F., Letocart, V., Gillotay, D., & Montmessin, F. (2017). Retrieving cloud, dust and ozone abundances in the Martian atmosphere using SPICAM/UV nadir spectra. *Planetary and Space Science*, *142*, 9–25. https://doi.org/10.1016/j.pss.2017.04.011

Wilson, R. J. (2002). Evidence for nonmigrating thermal tides in the Mars upper atmosphere from the Mars Global Surveyor Accelerometer Experiment. *Geophysical Research Letters*, *29*(7), 24–31. https://doi.org/10.1029/2001gl013975

Wolff, M. J., Bell, J. F., III., James, P. B., Clancy, R. T., & Lee, S. W. (1999). Hubble Space Telescope observations of the Martian aphelion cloud belt prior to the Pathfinder Mission: Seasonal and interannual variations. *Journal of Geophysical Research*, *104*(E4), 9027–9041. https://doi.org/10.1029/98je01967

Wolff, M. J., Clancy, R. T., Goguen, J. D., Malin, M. C., & Cantor, B. A. (2010). Ultraviolet dust aerosol properties as observed by MARCI. *Icarus*, *208*(1), 143–155. https://doi.org/10.1016/j.icarus.2010.01.010

Wolff, M. J., Clancy, R. T., Kahre, M. A., Haberle, R. M., Forget, F., Cantor, B. A., & Malin, M. C. (2019). Mapping water ice clouds on Mars with MRO/MARCI. *Icarus*, *332*, 24–49. https://doi.org/10.1016/j.icarus.2019.05.041

Wolff, M. J., Fernando, A., Smith, M. D., Forget, F., Millour, E., Atwood, S. A., et al. (2022). Diurnal variations in the aphelion cloud belt as observed by the Emirates Exploration Imager (EXI). *Geophysical Research Letters*, *49*(18), e2022GL100477. https://doi.org/10.1029/2022gl100477

Wolff, M. J., Smith, M. D., Clancy, R. T., Arvidson, R., Kahre, M., Seelos Iv, F., et al. (2009). Wavelength dependence of dust aerosol single scattering albedo as observed by the Compact Reconnaissance Imaging Spectrometer. *Journal of Geophysical Research*, *114*(E2). https://doi.org/10.1029/2009je003350